Journal of Fluids and Structures (2000) **14,** 443–468
doi:10.1006/jfls.1999.0281, available online at http://www.idealibrary.com on

SUPPRESSION OF VORTEX SHEDDING INSPIRED BY A LOW-DIMENSIONAL MODEL

S. Tang[1,2,†]
[1] *Department of Mechanical Engineering, New Jersey Institute of Technology*
Newark, NJ 07102, U.S.A.
[2] *Levich Institute and Department of Mechanical Engineering, The City College of*
New York, New York, NY 10031, U.S.A.

AND

N. Aubry[1,3]
[1] *Department of Mechanical Engineering, New Jersey Institute of Technology*
Newark, NJ 07102, U.S.A.
[3] *Department of Mathematics and Center for Applied Mathematics and Statistics,*
New Jersey Institute of Technology, Newark, NJ 07102, U.S.A.

(Received 5 July 1999, and in final form 9 November 1999)

In this paper, we show by two-dimensional numerical simulation that it is possible to control vortex shedding behind a circular cylinder by inserting two small vortex perturbations in the flow. The control has the effect of suppressing vortex shedding, making the flow converge toward a stable, symmetric bubble at Reynolds number $\mathrm{Re} = 100$. Similar results are obtained at higher Reynolds number values, e.g. $\mathrm{Re} = 1000$, although the required strength of the control vortices is higher than at $\mathrm{Re} = 100$. At all Reynolds numbers investigated here, it is also possible to choose the control parameters in order to alter vortex shedding by generating a reversed Karman vortex street. Our control technique is inspired by the linear stability analysis of a potential vortex model which we report in the present manuscript. The model is used here to give us insight into the control problem and the similarity between the model and the real, viscous flow remains qualitative. © 2000 Academic Press

1. INTRODUCTION

Vortex shedding control has been the object of intensive research over recent years. Arguments motivating the investigation of this issue are numerous. For instance, the shedding of vortices from alternate sides of bluff bodies is associated with strong periodic transverse forces that can damage the body. Preventing the instability from occurring would thus lead to the suppression of vortex-induced vibrations. It may also lead to drag reduction, a desired feature in many applications.

A wide variety of techniques have been applied, such as the use of a splitter plate (Roshko 1955; Grove *et al.* 1964), base bleed (Wood 1967; Bearman 1967), forced cylinder vibrations (Wehrmann 1965; Berger 1967; Schumm *et al.* 1994), wake heating (Noto *et al.* 1985; Mori *et al.* 1986), a small secondary cylinder (Strykowski & Sreenivasan 1990; Strykowski & Hannemann 1991), rotary oscillation of a cylinder (Tokumaru & Dimotakis 1991), and

---

† Current address: ABS Americas, Houston, TX 77060, U.S.A.

a flapping foil (Gopalkrishnan *et al.* 1994) among others [see, e.g., the review by Zdravkovich (1981)]. Feedback control techniques have also been developed (Ffowes Williams & Zhao 1989; Roussopoulos 1993). The list is by no means exhaustive, and the interested reader should consult the recent review on flow control by Gad-el-Hak (1999).

Some of these flow control techniques are successful at controlling or suppressing vortex shedding through a large modification (e.g. a splitter plate of length $10a$ or a flapping foil of chord $4a$, where a is the radius of the cylinder). Some other approaches, such as the insertion of a small cylinder in the wake, are small local modifications but are usually restricted to a small range of Reynolds numbers. In many cases, control techniques are empirical.

The implementation of an efficient control strategy requires the understanding of the origin of the physical phenomenon one wants to control. For this purpose, the derivation and analysis of a model, preferably a low-dimensional dynamical system which can capture the essential features of the physics and be understood relatively easily, should be of great help. During the last decade, the use of low-dimensional dynamical systems as powerful tools to model fluid mechanics phenomena has attracted much attention [see, for instance, Aubry *et al.* (1988), Sanghi & Aubry (1993), Coller *et al.* (1994)]. The present paper is based on such simple ideas applied to the origin of vortex shedding and its control.

Since vortex shedding is born through the instability of the recirculating bubble of counter-rotating, twin vortices, understanding the origin of vortex shedding should necessarily involve the investigation of the instability the symmetric bubble undergoes. We have recently studied the stability property of the recirculating bubble by reconsidering the low-dimensional, point vortex model first derived by Föppl (1913). This model consists of a uniform oncoming flow, a pair of point vortices symmetrically located with respect to the centerline behind the cylinder, and inner vortices placed to satisfy the boundary condition on the body. Föppl found steady solutions of this model and studied their linear stability with respect to *particular* perturbations. We have carried out the stability analysis with respect to *any* type of perturbations and have found the explicit shape of the eigenvector associated with each eigenvalue (Tang & Aubry 1997). The result of our analysis is that the steady pair of twin vortices is stable to some asymmetric perturbation, and unstable to some other asymmetric perturbation. The specific shape of the asymmetric perturbation responsible for the instability is thus crucial. We have then shown that the stability properties of the model mimic the stability characteristics of the wake flow simulated by numerical integration of the Navier–Stokes equations. In other words, a perturbation along the stable subspace of the model decays, while a perturbation along the unstable subspace is amplified.

After understanding the nature of the instability, one seeks to control it. In this paper, we investigate whether the linear instability can be suppressed in the model. We show here that this is possible by adding two small, fixed control point vortices. We then show that the insertion of additional small sources of vorticity also affects the numerically simulated viscous flow. Our idea of controlling a wake flow potential model is similar to that explored by Cortelezzi *et al.* (1994), Cortelezzi (1996) for the control of wake flows past a plate.

Our paper is organized as follows. In Sections 2 and 3, we recall the point vortex model, its linear stability analysis and its relation with the numerically simulated flow. In Section 4, we introduce two small control vortices in the model and find that this insertion is responsible for the presence of a neutrally stable equilibrium point. We then turn to the numerical simulation of the viscous flow past a cylinder in Section 5 and show that the introduction of vorticity sources in the flow can either suppress vortex shedding or generate a reversed Karman vortex street. We finally discuss our findings and conclude in Section 6.

2. MODEL FOR THE INSTABILITY OF THE SYMMETRIC BUBBLE

It is well known that if a circular cylinder starts moving from rest, twin vortices spinning in opposite direction form behind the cylinder soon after the motion begins. These vortices grow and become more and more elongated as time increases until they reach their maximal size. At low Reynolds number, the asymptotic state consists of a two-dimensional elongated bubble which is stable and invariant under reflection symmetry through the centerline, that is it satisfies $u(x, y, t) = u(x, -y, t), v(x, y, t) = -v(x, y, t)$ at *any* time. The bubble of vortices develops into a time-dependent oscillating wake regime in which the bubble remains attached to the body at about $\mathrm{Re} = 48$–50 or breaks down into a Karman vortex street at higher Reynolds number. Here, the previous *instantaneous* symmetry is broken, but the flow satisfies a space–time symmetry group in the sense that $u(x, y, t) = u(x, -y, t + T/2), v(x, y, t) = -v(x, -y, t + T/2)$, where T is the time period of the flow. In other words, one has to act on both the time and space variables in order to recover the invariance of the flow, see more details on this particular symmetry, as well as other space–time symmetries in Aubry *et al.* (1992), Aubry & Lima (1995). In this paper, we concentrate on the *instantaneous* symmetry-breaking instability and its control.

In order to understand the (instantaneous) symmetry-breaking instability, we have modeled the symmetric bubble by means of twin-point vortices behind the cylinder, two inner vortices placed to satisfy the boundary condition on the body and the uniform oncoming flow (Föppl 1913; Tang & Aubry 1997). The twin-point vortices behind the body are symmetric images of one another by reflection through the centerline. A sketch of the model can be found in Figure 1(a), which also shows the location of the steady solutions on two (symmetric) curves. The linear stability analysis (Tang & Aubry 1997) shows that the four-dimensional dynamical system has one strictly positive eigenvalue, $\lambda_1 > 0$, one strictly negative eigenvalue $\lambda_2 < 0$ and two eigenvalues, λ_3 and λ_4, whose real parts are zero. The unstable and stable eigenvectors take the following expressions:

$$\mathbf{V}_1 = \begin{Bmatrix} \alpha \\ 1 \\ -\alpha \\ 1 \end{Bmatrix}, \quad \mathbf{V}_2 = \begin{Bmatrix} -\beta \\ 1 \\ \beta \\ 1 \end{Bmatrix}, \tag{1}$$

where α and β are positive real numbers. The eigenvectors corresponding to $\lambda_{3,4}$ in the real space span a symmetric center eigenspace. Figure 1(b) shows that the eigenvalue λ_1 decays rapidly to zero with the distance $r_1 = \sqrt{x_1^2 + y_1^2}$ of the vortices to the center of the body. In Figure 1(c), we have sketched the mode $\mathbf{V}_1$ spanning the unstable eigenspace, the mode $\mathbf{V}_2$ spanning the stable eigenspace, and the modes $\mathbf{V}_3$ and $\mathbf{V}_4$ spanning the center eigenspace. Owing to their shapes, $\mathbf{V}_1$ and $\mathbf{V}_2$ are referred to as the *asymmetric divergent* mode and the *asymmetric convergent* mode, respectively. Similarly, $\mathbf{V}_3$ is called the *symmetric divergent* mode and $\mathbf{V}_4$ the *symmetric convergent* mode. In the next section, we show the relation between this finding and the symmetry-breaking instability in the numerically simulated viscous flow (Tang & Aubry 1997). The numerical test consists in inserting a small vorticity perturbation on the centerline either very close to the body or far away downstream. In the first case, the induced velocity perturbation on the twin vortices is close to the stable eigenmode $\mathbf{V}_2$, as shown in Figure 2(a), while in the second case, it is close to the unstable eigenmode $\mathbf{V}_1$, as sketched in Figure 2(b).

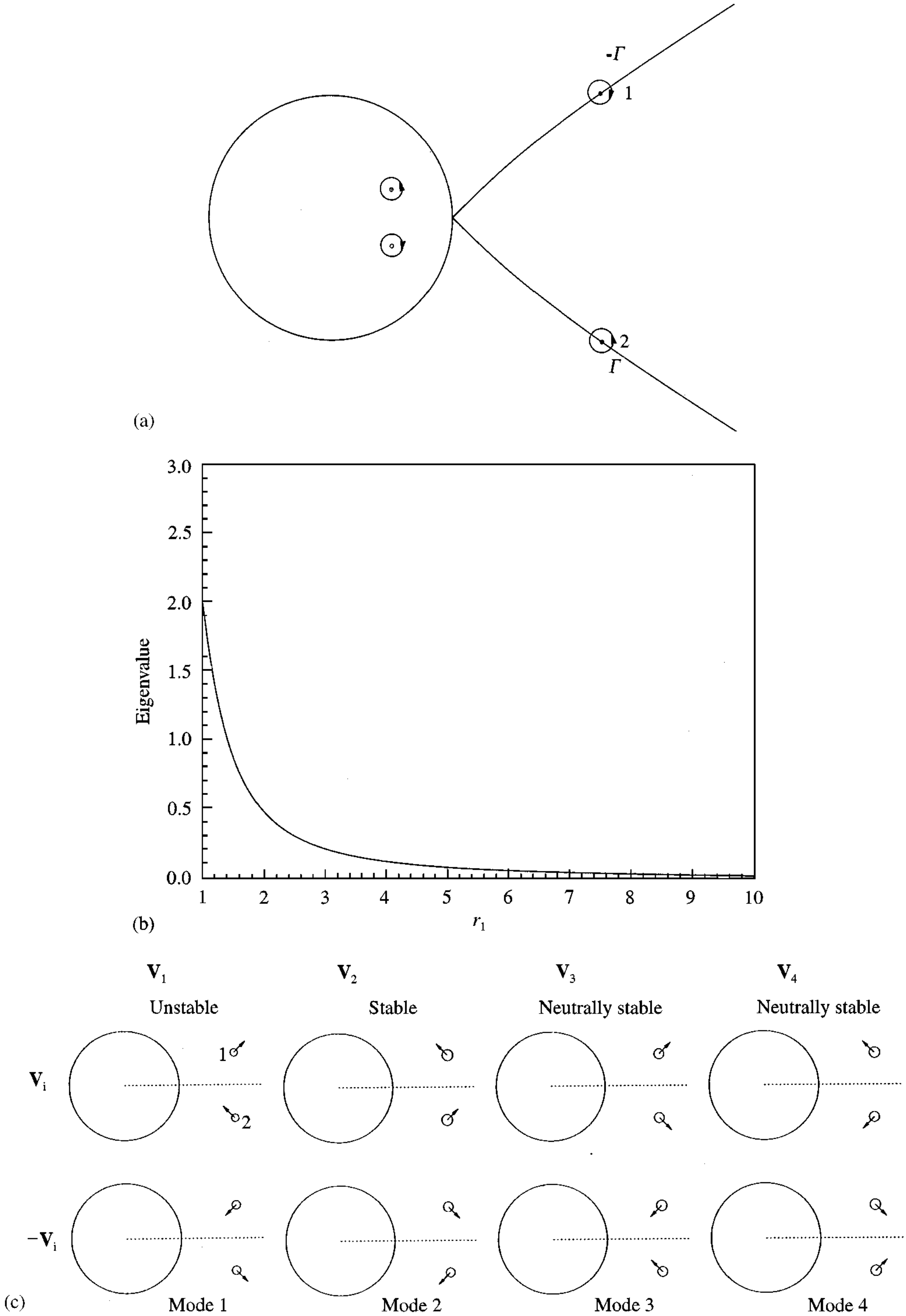

Figure 1. Low-dimensional model representing twin point vortices and their stability property behind a circular cylinder: (a) sketch of the symmetric vortex pair and plot of the curve of equilibria in the model; (b) absolute value of the unstable and stable eigenvalues λ_1, λ_2 ($= -\lambda_1$) as a function of the distance r_1 to the center of the cylinder; (c) configuration of the four vectors $\mathbf{V}_1$, $\mathbf{V}_2$, $\mathbf{V}_3$ and $\mathbf{V}_4$ (top) and their opposite companions $-\mathbf{V}_1$, $-\mathbf{V}_2$, $-\mathbf{V}_3$ and $-\mathbf{V}_4$ (bottom) [from Tang & Aubry (1997)].

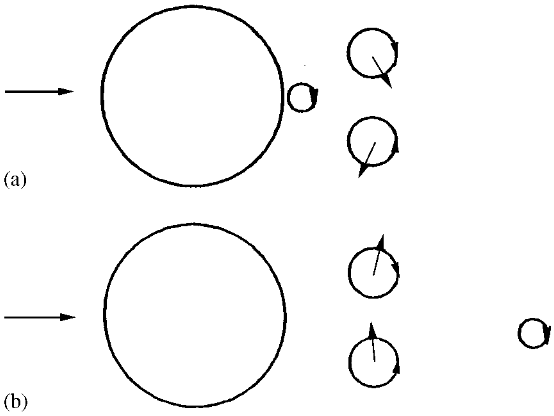

Figure 2. Sketch showing the small vorticity perturbation introduced in the flow and the two main twin vortices of the recirculating bubble: (a) the perturbation is close to the cylinder, so that the associated velocity disturbance applied to the twin vortices is of the asymmetric *convergent* type; (b) the perturbation is far away from the cylinder, so that the associated velocity disturbance is of the asymmetric *divergent* type.

3. NUMERICAL SIMULATIONS

Before presenting our test on the flow stability, we recall our numerical simulation of the impulsively started flow past a circular cylinder.

3.1. Simulation Methodology

The governing equations considered in this paper are the two-dimensional, incompressible Navier–Stokes equations in the vorticity/streamfunction formulation. A finite difference method is used to simulate the flow in an exponential-polar coordinate system (ξ, η) defined by $\tilde{r} = a\mathrm{e}^{2\pi\xi}$ and $\tilde{\theta} = 2\pi\eta$, where $(\tilde{r}, \tilde{\theta})$ are the polar coordinates. This exponential mapping allows the code to deal with a very large physical domain so that the well-known blockage effect can be avoided. The Navier–Stokes equations are subject to the no-slip boundary conditions on the surface of the body and the two-dimensional potential flow at infinity. The impulsive start is simulated by imposing the potential flow as the initial condition everywhere, except on the body. Our scheme is adaptive in the sense that the boundary for the vorticity transport equation moves farther and farther away from the body as the vorticity is transported outward. The numerical scheme, second-order in space and first-order in time, is an alternating-direction-implicit (ADI) algorithm for the vorticity transport equation and a fast Fourier transform for the Poisson equation. The grid chosen in this paper has, unless specified otherwise, 1200×512 points and double precision is used. Details of the numerical method can be found in Tang & Aubry (1997). Our results at Reynolds number $\mathrm{Re} = 20, 40, 100, 500, 1000$, are in very good agreement with others' theoretical results (Collins & Dennis 1973; Bar-Lev & Yang 1975), experimental results (Tritton 1959; Williamson 1995) and numerical results (Zhang *et al.* 1995; Franke *et al.* 1990) for both the transient flow and the asymptotic regime. For instance, Figure 3 shows the time history of the drag coefficient at early times and the vorticity contours of the Karman vortex street at $\mathrm{Re} = 100$. Our findings agree with the theoretical results of Collins & Dennis (1973) and Bar-Lev & Yang (1975) for the early stage and with the Digital Particle Image

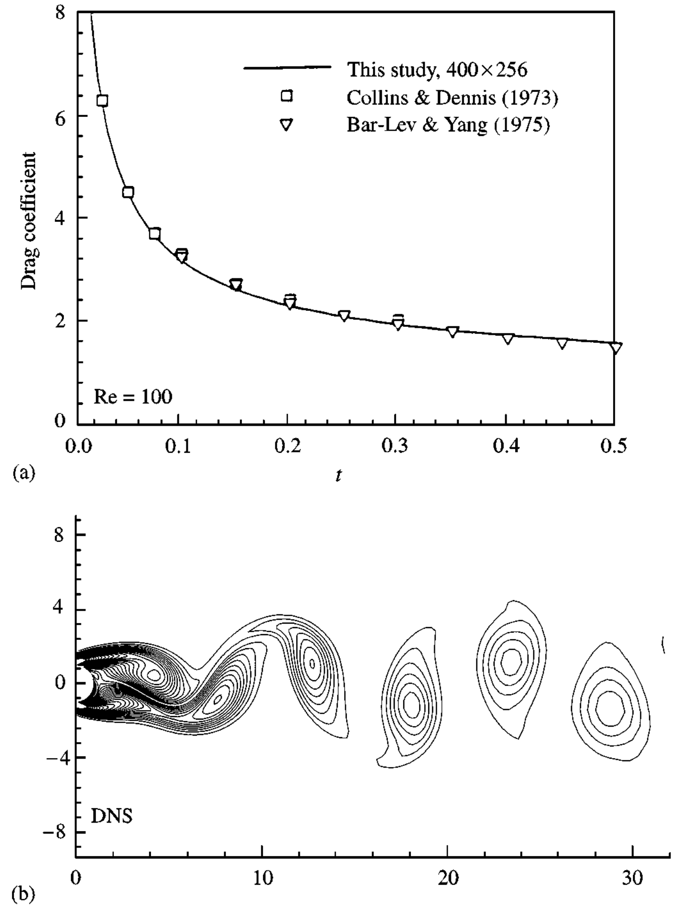

Figure 3. Flow at Re = 100: (a) drag coefficient versus time from this study and comparison with others' results; (b) vorticity contour plot for $-2{\cdot}5 \leqslant \omega \leqslant 2{\cdot}5$, with a spacing of 0.1 at time $t = 650$, visualizing the Karman vortex street. The plot shows a remarkable agreement with those computed by Henderson (1994); see also Williamson (1995).

Velocimetry (DPIV) measurements of Gharib, Hammache, Maheo and Dabri and the numerical computations of Henderson (1994) [see also Williamson (1995)]. The mean value of the drag coefficient, the amplitude of the lift coefficient and the Strouhal number in the Karman vortex street can be found in Tang & Aubry (1997). They all compare well with other numerical and experimental data.

We use two distinct algorithms for computing the forces exerted on the body, which we now discuss.

3.1.1. Algorithm 1

The time-dependent drag coefficient (C_d) and lift coefficient (C_l) on the body can be computed according to the formulation

$$-C_d(t) + \mathrm{i}C_l(t) = \frac{2}{\mathrm{Re}}\,\mathrm{i}\int_0^1 \mathrm{e}^{\mathrm{i}2\pi\eta}\left[2\pi\omega(t) - \frac{\partial\omega}{\partial\xi}(t)\right]_{\xi=0} \mathrm{d}\eta. \tag{2}$$

This formula can be easily implemented since we know the vorticity field at each time step.

3.1.2. *Algorithm 2*

The body force can also be computed from the control volume formulation of the momentum equation. Hereafter, *cv* and *cs* refer to the control volume and the control surface, respectively. Our control volume is chosen to be a coaxial cylinder of large radius containing the body. The net force exerted on the body by the fluid can then be expressed as

$$\mathbf{F}_s = \mathbf{F}_{cs} - \frac{\mathrm{d}}{\mathrm{d}t}\iint_{cv} \mathbf{u}\rho\,\mathrm{d}v - \int_{cs} \mathbf{u}\rho\mathbf{u}\cdot\mathbf{n}\,\mathrm{d}s, \qquad (3)$$

where $\mathbf{F}_{cs}$ denotes the surface force. Note that this technique requires the knowledge of the full velocity field in the control volume, while the vorticity flux is needed only on the control surface.

3.2. Stability Property of the Numerically Simulated Flow

In this paragraph, we recall results obtained in Tang & Aubry (1997). We introduce vorticity perturbations in the flow in the manner described in Figure 2 (see Section 2). Our numerical tests are performed at Re = 56. The first experiment consists in introducing a vorticity perturbation of circulation $\Gamma_p = \omega_p \mathrm{d}A = 0{\cdot}003$ at time $t = 100$ at the location $(1{\cdot}1, 0{\cdot}0)$ on the centerline, and relaxing it immediately after this. We recall that the induced velocity perturbation on the twin vortices is close to the stable eigenmode $\mathbf{V}_2$ of the model.

The second experiment consists in introducing the same vorticity perturbation in the flow, but much farther downstream, that is at the location $(10{\cdot}1, 0{\cdot}0)$. In this case, the induced velocity perturbation on the twin vortices is close to the unstable eigenmode $\mathbf{V}_1$ of the model. Figure 4 shows the time history of the lift coefficient without perturbation and with the two types of perturbations previously described. It is clear that the upstream perturbation decays while the downstream one grows. Consequently, the downstream perturbation having a non-zero component along the unstable eigenvector $\mathbf{V}_1$ triggers the instability, thus showing the similarity between the stability property of the model and that of the numerically simulated flow. In the next sections, we concentrate on controlling the instability first in the model and secondly in the viscous flow.

4. CONTROL MODEL FOR THE SYMMETRY-BREAKING INSTABILITY

In order to control the linear instability of the vortices in the model of Section 2, we recall that the unstable eigenspace is one-dimensional and that the corresponding (real) eigenvalue tends to zero rapidly as the distance of the vortices from the center of the cylinder increases [see Figure 1(b)]. This point leads us to wonder whether one can use a small effort to change the sign of the square of the eigenvalues $\lambda_{1,2}^2$ from positive to negative in order to eliminate the unstable eigenspace and therefore neutrally stabilize the symmetric bubble of vortices.

4.1. Control Model and Its Stability Analysis

A control approach is investigated by designing a new dynamical system consisting of the previous vortex model to which we add a pair of symmetric control vortices that are

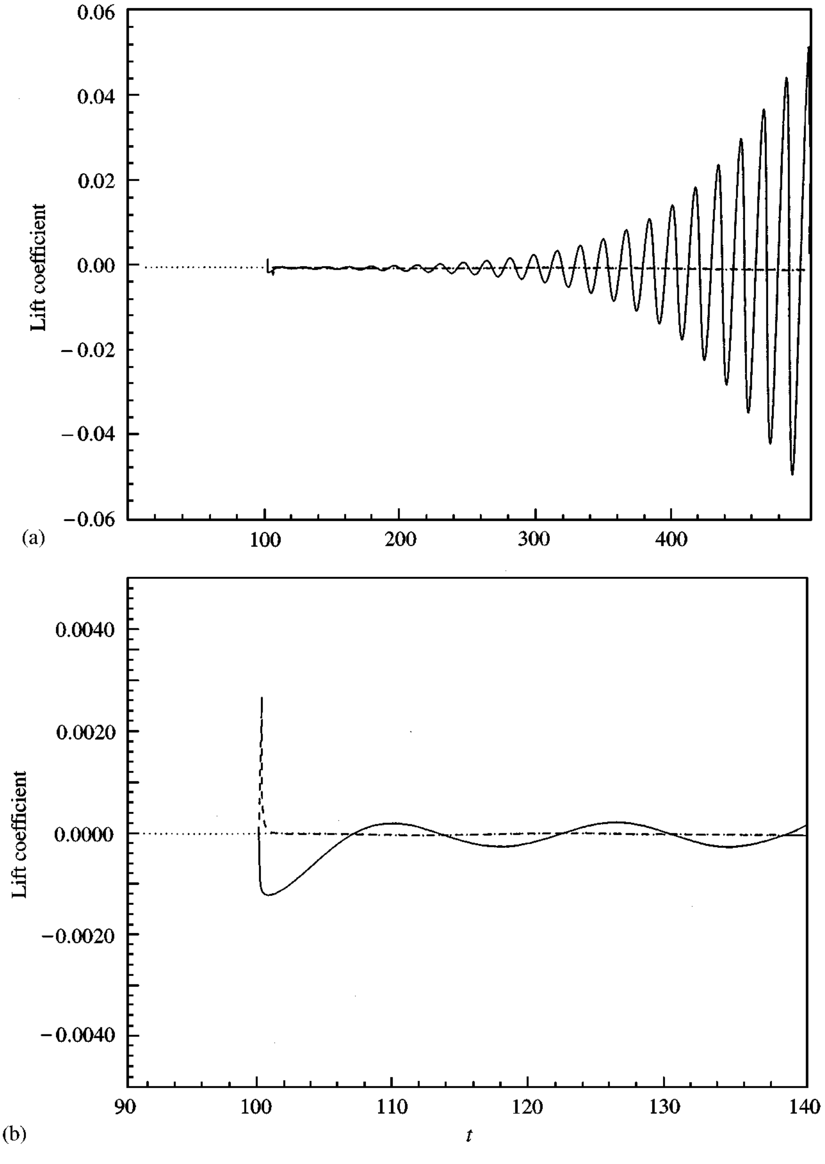

Figure 4. Time history of the lift coefficient from the numerical simulation at Re = 56: (i) without any artificial perturbation (dotted line), (ii) with the vorticity perturbation introduced at $x_1 = 10{\cdot}1$ (solid line), and (iii) with the vorticity perturbation introduced at $x_1 = 1{\cdot}1$ (dashed line). (a) Lift coefficient; (b) zoom of (a). It is clear that the asymmetric divergent perturbation grows while the asymmetric convergent perturbation decays [from Tang & Aubry (1997)].

maintained at the locations $z_c = x_c + \mathrm{i}y_c$ and $\bar{z}_c$, respectively (see Figure 5). Hereafter, Γ_c denotes the circulation of the upper control vortex, $-\Gamma_c$ being the circulation of the lower control vortex ($\Gamma_c > 0$). The original vortices located at z_1 and z_2, of circulation $-\Gamma$ and Γ ($\Gamma > 0$) , respectively, are referred to as the *twin vortices*, since they represent the recirculating bubble in the real flow. Under the assumption that the velocity of the oncoming flow is $U_\infty = 1$ and that the radius of the cylinder is also equal to 1, the new

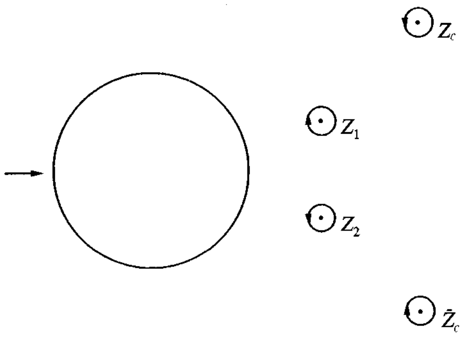

Figure 5. Sketch showing the twin vortices at positions z_1 and z_2 and the control vortices located at positions z_c and $\bar{z}_c$ in the control model.

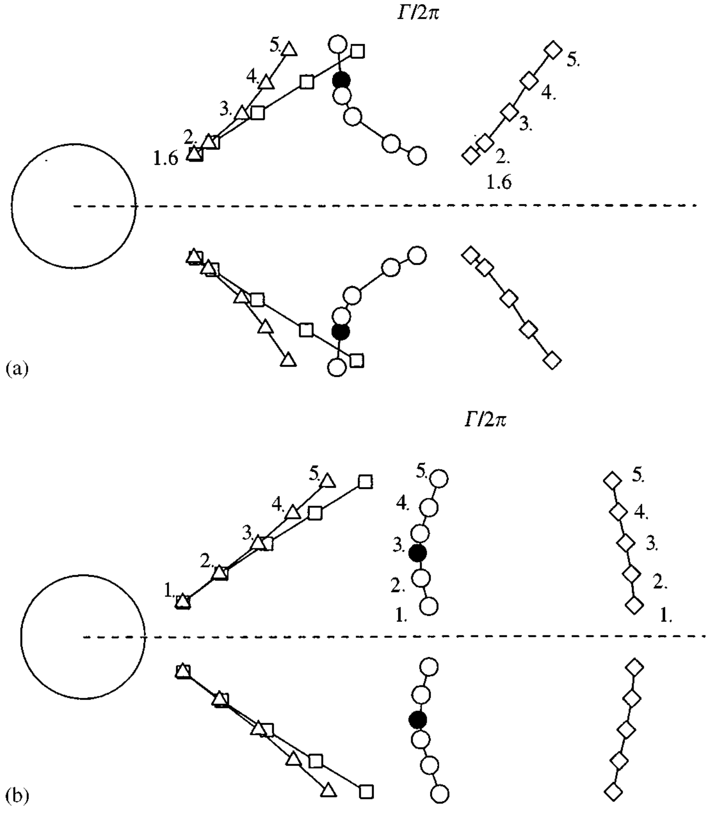

Figure 6. Location of the equilibrium positions for the control model whose control vortices have a circulation equal to $\Gamma_c/2\pi = 0{\cdot}03$: (a) the control vortices are located at $x_c = 4{\cdot}294$, $y_c = \pm 2{\cdot}031$; (b) the control vortices are located at $x_c = 5{\cdot}392$, $y_c = \pm 1{\cdot}35$. Equilibrium curve of the (uncontrolled) original model (squares), equilibrium curve 1 (triangles), equilibrium curve 2 (circles), equilibrium curve 3 (diamonds). We have indicated the values of the circulation $\Gamma/2\pi$ of the twin vortices corresponding to each equilibrium.

four-dimensional dynamical system (whose variables are $z_1 = x_1 + \mathrm{i}y_1$ and $z_2 = x_2 + \mathrm{i}y_2$) is given by the equations

$$\begin{aligned}\frac{\mathrm{d}\bar{z}_1}{\mathrm{d}t} = 1 - \frac{1}{z_1^2} &+ \frac{\Gamma}{2\pi\mathrm{i}}\frac{1}{z_1 - 1/\bar{z}_1} - \frac{\Gamma}{2\pi\mathrm{i}}\frac{1}{z_1 - 1/\bar{z}_2} + \frac{\Gamma}{2\pi\mathrm{i}}\frac{1}{z_1 - z_2}\\ &+ \frac{\Gamma_c}{2\pi\mathrm{i}}\frac{1}{z_1 - z_c} - \frac{\Gamma_c}{2\pi\mathrm{i}}\frac{1}{z_1 - \bar{z}_c} - \frac{\Gamma_c}{2\pi\mathrm{i}}\frac{1}{z_1 - 1/\bar{z}_c} + \frac{\Gamma_c}{2\pi\mathrm{i}}\frac{1}{z_1 - 1/z_c},\end{aligned} \tag{4}$$

$$\begin{aligned}\frac{\mathrm{d}\bar{z}_2}{\mathrm{d}t} = 1 - \frac{1}{z_2^2} &- \frac{\Gamma}{2\pi\mathrm{i}}\frac{1}{z_2 - 1/\bar{z}_2} + \frac{\Gamma}{2\pi\mathrm{i}}\frac{1}{z_2 - 1/\bar{z}_1} - \frac{\Gamma}{2\pi\mathrm{i}}\frac{1}{z_2 - z_1}\\ &+ \frac{\Gamma_0}{2\pi\mathrm{i}}\frac{1}{z_2 - z_c} - \frac{\Gamma_c}{2\pi\mathrm{i}}\frac{1}{z_2 - \bar{z}_c} - \frac{\Gamma_c}{2\pi\mathrm{i}}\frac{1}{z_2 - 1/\bar{z}_c} + \frac{\Gamma_c}{2\pi\mathrm{i}}\frac{1}{z_2 - 1/z_c}.\end{aligned} \tag{5}$$

Here z_2 should be replaced by $\bar{z}_1$ for symmetric solutions, particularly for symmetric fixed points. The second equation of motion is identical to the first one in which z_1 is replaced by z_2, Γ by $-\Gamma$ and *vice versa.*

The control system is more complex than the original model of Section 2 due to the fact that it has three extra independent parameters, which are the characteristics of the control vortices x_c, y_c and Γ_c. Since it is beyond the scope of this work to study the dynamics in this three-dimensional parameter space, we restrict our analysis to a few relevant cases.

We concentrate on finding the symmetric equilibria of the new model by solving the equations $\mathrm{d}\bar{z}_1/\mathrm{d}t = 0$, $z_2 = \bar{z}_1$, (where $\mathrm{d}\bar{z}_1/\mathrm{d}t$ is given by equation (4)], the characteristics x_c, y_c and Γ_c of the control vortices and the circulation Γ of the twin vortices being considered as parameters. For this, we proceed as follows. Given x_c, y_c, Γ_c and Γ, we obtain the real part, u, and the imaginary part, v, as functions of x_1 and y_1, from the right-hand side of equations (4) and (5). We then plot the zero streamwise and zero transverse velocity lines corresponding to $u = 0$ and $v = 0$, respectively. The equilibria we are seeking are located at the intersection points between the two curves. We observe that if Γ_c is too small, there is only one equilibrium similar to that of the original vortex model, and its stability properties are the same as those described in Section 2. If Γ_c is increased, but still small compared to Γ, the control vortex model generates (at least) three equilibria. Figure 6(a) shows the three curves of equilibria corresponding to the set of parameters $(x_c, y_c) = (4{\cdot}294, 2{\cdot}031)$, $\Gamma_c/2\pi = 0{\cdot}03$ and different values of $\Gamma/2\pi$ ($\Gamma/2\pi = 1{\cdot}6, 2, 3, 4, 5$). The curves represented by triangles, circles, diamonds are referred to as Curve 1, Curve 2 and Curve 3, respectively. The squares correspond to the equilibria of the original model. Curve 1 is analogous to the curve of fixed points obtained in the original point vortex model of Section 2. The other two points are new equilibria strictly due to the presence of the control vortices. Figure 6(b) shows similar results for the set of parameters $(x_c, y_c) = (5{\cdot}392, 1{\cdot}35)$, $\Gamma_c/2\pi = 0{\cdot}03$ and different values of $\Gamma/2\pi$ ($\Gamma/2\pi = 1, 2, 3, 4, 5$).

We now carry out the linear stability analysis of the fixed points and derive the equations of motion governing the dynamics of the perturbations around each equilibrium. Hereafter, x_1, y_1 denote the coordinates of the fixed point considered. The linear dynamics of the perturbation is governed by the set of ordinary differential equations (ODE):

$$\frac{\mathrm{d}}{\mathrm{d}t}\begin{Bmatrix} x_1' \\ y_1' \\ x_2' \\ y_2' \end{Bmatrix} = \begin{bmatrix} A & B & c & d \\ E & -A & f & c \\ c & -d & A & -B \\ -f & c & -E & -A \end{bmatrix}\begin{Bmatrix} x_1' \\ y_1' \\ x_2' \\ y_2' \end{Bmatrix}, \tag{6}$$

where

$$A(x_1) = a(x_1) + P_r(x_1), \tag{7}$$

$$B(x_1) = b(x_1) - P_i(x_1), \tag{8}$$

$$E(x_1) = e(x_1) - P_i(x_1), \tag{9}$$

with

$$\begin{aligned} P_r(x_1) + \mathrm{i}P_i(x_1) = {} & -\frac{\Gamma_c}{2\pi \mathrm{i}} \frac{1}{(z_1 - z_c)^2} + \frac{\Gamma_c}{2\pi \mathrm{i}} \frac{1}{(z_1 - \bar{z}_c)^2} \\ & + \frac{\Gamma_c}{2\pi \mathrm{i}} \frac{1}{(z_1 - 1/\bar{z}_c)^2} - \frac{\Gamma_c}{2\pi \mathrm{i}} \frac{1}{(z_1 - 1/z_c)^2}, \end{aligned} \tag{10}$$

$$a(x_1) = \frac{2(x_1^3 - 3x_1 y_1^2)}{r_1^6} + \frac{\Gamma x_1 y_1}{\pi(r_1^2 - 1)^2} - \frac{\Gamma x_1 y_1 (r_1^4 - 1)}{\pi[(x_1^2 - y_1^2 - 1)^2 + 4x_1^2 y_1^2]^2}, \tag{11}$$

$$\begin{aligned} \mathrm{b}(x_1) = {} & \frac{-2(y_1^3 - 3x_1^2 y_1)}{r_1^6} - \frac{\Gamma(x_1^2 - y_1^2)}{2\pi(r_1^2 - 1)^2} + \frac{\Gamma}{2\pi(r_1^2 - 1)^2} \\ & + \frac{\Gamma[x_1^2(r_1^2 - 1)^2 - y_1^2(r_1^2 + 1)^2]}{2\pi[(x_1^2 - y_1^2 - 1)^2 + 4x_1^2 y_1^2]^2} + \frac{\Gamma}{8\pi y_1^2}, \end{aligned} \tag{12}$$

$$c(x_1) = \frac{-2\Gamma x_1 y_1 (x_1^2 - y_1^2 - 1)}{\pi[(x_1^2 - y_1^2 - 1)^2 + 4x_1^2 y_1^2]^2}, \tag{13}$$

$$d(x_1) = \frac{-\Gamma[(x_1^2 - y_1^2 - 1)^2 - 4x_1^2 y_1^2]}{2\pi[(x_1^2 - y_1^2 - 1)^2 + 4x_1^2 y_1^2]^2} - \frac{\Gamma}{8\pi y_1^2}, \tag{14}$$

$$\begin{aligned} e(x_1) = {} & \frac{-2(y_1^3 - 3x_1^2 y_1)}{r_1^6} - \frac{\Gamma(x_1^2 - y_1^2)}{2\pi(r_1^2 - 1)^2} - \frac{\Gamma}{2\pi(r_1^2 - 1)^2} \\ & + \frac{\Gamma[x_1^2(r_1^2 - 1)^2 - y_1^2(r_1^2 + 1)^2]}{2\pi[(x_1^2 - y_1^2 - 1)^2 + 4x_1^2 y_1^2]^2} + \frac{\Gamma}{8\pi y_1^2}, \end{aligned} \tag{15}$$

$$f(x_1) = \frac{\Gamma[(x_1^2 - y_1^2 - 1)^2 - 4x_1^2 y_1^2]}{2\pi[(x_1^2 - y_1^2 - 1)^2 + 4x_1^2 y_1^2]^2} - \frac{\Gamma}{8\pi y_1^2}. \tag{16}$$

Note that A, B, c, d, E, f are functions of $r_1 = (x_1^2 + y_1^2)^{1/2}$ such that x_1 and y_1 are related (since they are the coordinates of one equilibrium). We then retain the x_1-dependency only, i.e. $A(x_1)$, $B(x_1)$, $c(x_1)$, $d(x_1)$, $E(x_1)$, $f(x_1)$. While such dependency should be kept in mind, it is often dropped to lighten the notation. Here, a, b, c, d, e and f are related to the twin vortices as they are in the original vortex model of Section 2, while the existence of the extra terms P_r and P_i is strictly due to the control vortices. The Jacobian matrix of equation (6) reduces to the Jacobian matrix of the original model if P_r and P_i are set to zero.

We now diagonalize the Jacobian matrix and obtain the following eigenvalues and eigenvectors

$$(\lambda^c_{1,2})^2 = (A - c)^2 + (B + d)(E - f), \quad \mathbf{V}^c_{1,2} = \begin{Bmatrix} \dfrac{B + d}{\lambda_{1,2} - A + c} \\ 1 \\ \dfrac{-(B + d)}{\lambda_{1,2} - A + c} \\ 1 \end{Bmatrix} \tag{17}$$

$$(\lambda^c_{3,4})^2 = (A + c)^2 + (B - d)(E + f), \quad \mathbf{V}^c_{3,4} = \begin{Bmatrix} \dfrac{d - B}{\lambda_{3,4} - A - c} \\ -1 \\ \dfrac{d - B}{\lambda_{3,4} - A - c} \\ 1 \end{Bmatrix}. \tag{18}$$

We can rewrite the eigenvalues as

$$(\lambda^c_{1,2})^2 = (a - c)^2 + (b + d)(e - f) + P_r^2 + P_i^2 + 2(a - c)P_r - P_i(b + d + e - f), \tag{19}$$

$$(\lambda^c_{3,4})^2 = (a + c)^2 + (b - d)(e + f) + P_r^2 + P_i^2 + 2(a + c)P_r - P_i(b - d + e + f). \tag{20}$$

As expected, the eigenvalues (20) and (21) coincide with the eigenvalues of the original model if P_r and P_i are set to zero. The extra terms due to the presence of the control vortices involve both P_r and P_i which are proportional to the circulation Γ_c of the control vortices. Our aim is now to make $(\lambda^c_{1,2})^2$ negative in order to eliminate the one-dimensional unstable eigenspace of the original model (while keeping $(\lambda^c_{3,4})^2$ negative). One can see that this goal may be reached if the circulation Γ_c of the control vortices is not too small.

The stability analysis of the three previous equilibria corresponding to the set of parameters $(x_c, y_c) = (2{\cdot}908, 1{\cdot}375)$, $\Gamma_c/2\pi = 0{\cdot}048$ and $\Gamma/2\pi = 1{\cdot}6$ is summarized below.

Equilibrium 1:

$$\lambda^c_1 = 0{\cdot}4504, \quad \mathbf{V}^c_1 = \begin{Bmatrix} 0{\cdot}6559 \\ 1 \\ -0{\cdot}6559 \\ 1 \end{Bmatrix}, \quad \textit{unstable subspace}, \tag{21}$$

$$\lambda^c_2 = -0{\cdot}4504, \quad \mathbf{V}^c_2 = \begin{Bmatrix} -0{\cdot}2174 \\ 1 \\ 0{\cdot}2174 \\ 1 \end{Bmatrix}, \quad \textit{stable subspace}, \tag{22}$$

$$(\lambda^c_{3,4})^2 = -0{\cdot}4056, \quad \textit{center subspace}. \tag{23}$$

Equilibrium 2:

$$\lambda_1^c = 0{\cdot}3422, \quad \mathbf{V}_1^c = \begin{Bmatrix} 0{\cdot}2168 \\ 1 \\ -0{\cdot}2168 \\ 1 \end{Bmatrix}, \quad \textit{unstable subspace}, \tag{24}$$

$$\lambda_2^c = -0{\cdot}3422, \quad \mathbf{V}_2^c = \begin{Bmatrix} -0{\cdot}2849 \\ 1 \\ 0{\cdot}2849 \\ 1 \end{Bmatrix}, \quad \textit{stable subspace}, \tag{25}$$

$$\lambda_3^c = 0{\cdot}3183, \quad \mathbf{V}_3^c = \begin{Bmatrix} -3{\cdot}6037 \\ -1 \\ -3{\cdot}6037 \\ 1 \end{Bmatrix}, \quad \textit{unstable subspace}, \tag{26}$$

$$\lambda_4^c = -0{\cdot}3183, \quad \mathbf{V}_4^c = \begin{Bmatrix} 5{\cdot}7692 \\ -1 \\ 5{\cdot}7692 \\ 1 \end{Bmatrix}, \quad \textit{stable subspace}, \tag{27}$$

Equilibrium 3:

$$(\lambda_{1,2}^c)^2 = -0{\cdot}003473, \quad \textit{center subspace}, \tag{28}$$

$$(\lambda_{3,4}^c)^2 = -0{\cdot}00527, \quad \textit{center subspace}. \tag{29}$$

In conclusion, the stability characteristic of Equilibrium 1 is similar to the stability of the unique equilibrium of the original model (Section 2) : both fixed points have one positive eigenvalue, one negative eigenvalue and two conjugate imaginary eigenvalues. The unstable subspace consists of the asymmetric divergent mode, while the asymmetric convergent mode characterizes the stable subspace. The center subspace is spanned by two symmetric modes. Equilibrium 2 has two unstable eigenspaces, spanned by the asymmetric divergent mode and the symmetric divergent mode, and two stable eigenspaces spanned by the asymmetric convergent and symmetric convergent modes. Finally, all the eigenvalues of Equilibrium 3 are imaginary. Here, both the stable and unstable eigenspaces disappear and the center subspace is four-dimensional. The existence of the third equilibrium shows that a small control vortex couple can (neutrally) stabilize a symmetric bubble.

The stability analysis has been performed with all the parameter values, x_c, y_c, Γ_c and Γ given in Table 1.

In *all* these cases, the stability properties of the control model are qualitatively the same as those previously described, that is the equilibria located on Curves 1 and 2 are found to be unstable while the equilibria of Curve 3 are neutrally stable. The existence of a neutrally stable equilibrium is robust in the sense that it is valid for a wide range of parameters in the model.

These stability features of the control model are confirmed by the following numerical integration of equations (4) and (5).

Table 1

Parameter values used for the integration of the control model

(x_0, y_0)	$\Gamma_0/2\pi$	$\Gamma/2\pi$
(2·908, 1·375)	0·048	1·6
(2·908, 1·375)	0·096	1·6
(4·908, 1·375)	0·048	1·6
(2·908, 1·375)	0·03	2
(2·908, 1·375)	0·05	2
(4·294, 2·031)	0·03	1·6
(4·294, 2·031)	0.03	2
(4·294, 2·031)	0·03	3
(4·294, 2·031)	0·03	4
(4·294, 2·031)	0·03	5
(5·392, 1·35)	0·03	1
(5·392, 1·35)	0·03	2
(5·392, 1·35)	0·03	3
(5·392, 1·35)	0·03	4
(5·392, 1·35)	0.03	5

4.2. INTEGRATION OF THE CONTROL MODEL

In order to illustrate the existence of the equilibria, their stability and the role they play in the solutions of the (non-linear) model, we integrate the ordinary differential equations (4) and (5), starting with various initial conditions. The numerical simulations are performed by means of a fourth-order Runge–Kutta integration method used with double precision. In the simulations, we have chosen the parameter values $(x_0, y_0) = (2{\cdot}908, 1{\cdot}375)$, $\Gamma_0/2\pi = 0{\cdot}048$ and $\Gamma/2\pi = 1{\cdot}6$ for the location, the circulation of the control vortices and the circulation of the twin vortices, respectively. Note that the linear stability analysis has also been performed for these parameter values (see Section 4.1 and Table 1).

4.2.1. Dynamics in the symmetric subspace

Figure 7(a) shows the trajectories obtained with initial conditions consisting *of symmetric* perturbations to the equilibria. One can clearly see, in this symmetric subspace, that Equilibria 1 and 3 are centers while Equilibrium 2 is a saddle point stable to symmetric convergent perturbations and unstable to symmetric divergent perturbations. These stability features coincide with our previous theoretical analysis. Starting with an initial condition close to Equilibrium 2 also shows the existence of a homoclinic cycle connecting the saddle to itself and wondering around the two centers. The remaining trajectories are limit cycles wandering around each center or around the homoclinic cycle. Figure 7(b) confirms this picture by providing a zoom of the top-half of Figure 7(a).

4.2.2. Dynamics in the full space

Our linear stability analysis has shown that Equilibria 1 and 2 are unstable to some asymmetric perturbations and Equilibrium 3 is neutrally stable to *all* kinds of perturbations. This is corroborated by integrating the original non-linear equations and by computing the trajectory of the vortices. The latter which are given small *asymmetric* perturbations

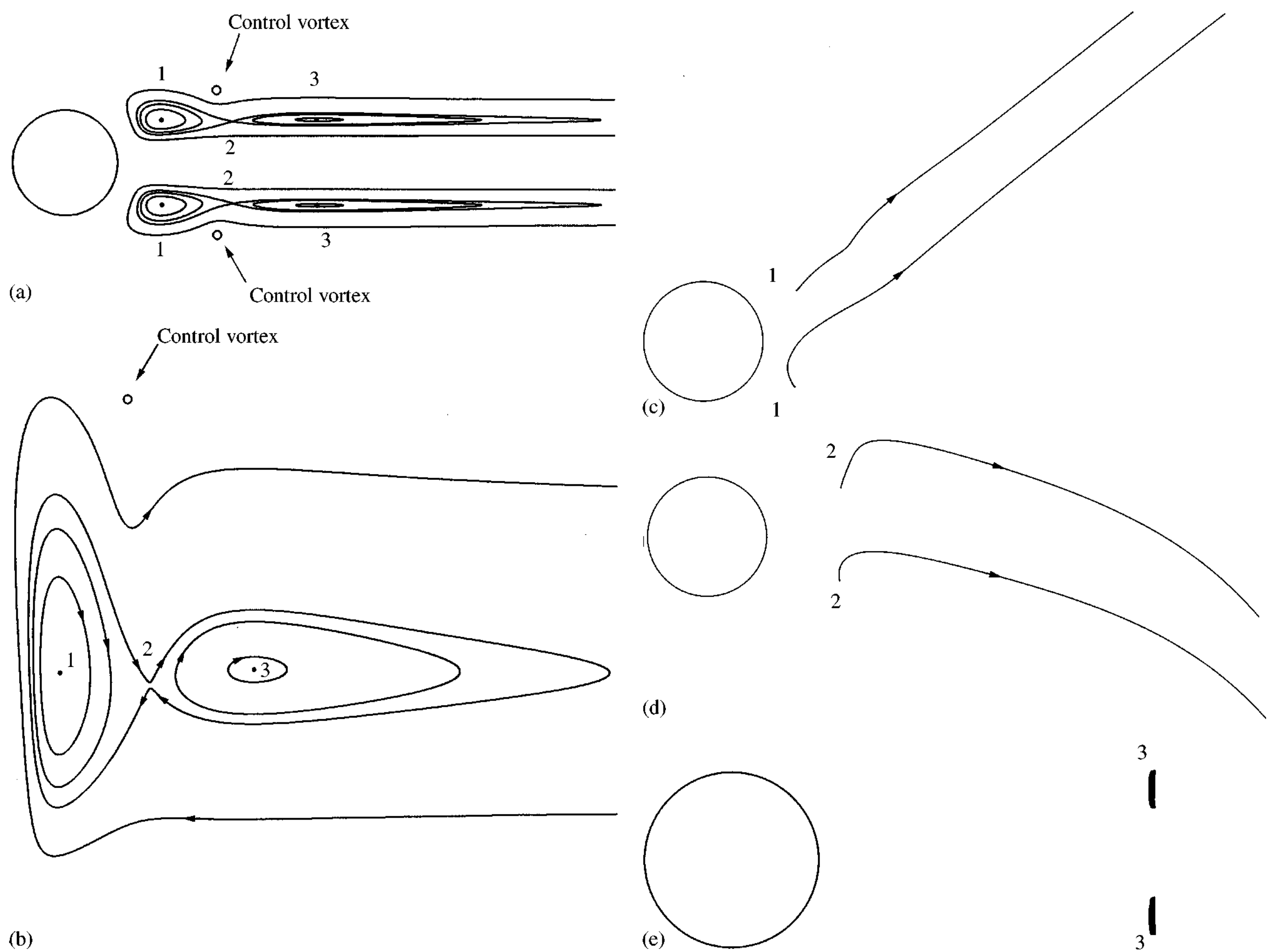

Figure 7. Representation of the cylinder and the trajectory of the point vortices solutions of the low-dimensional control model (5) whose parameters are $x_c = 2{\cdot}908$, $y_c = \pm 1{\cdot}375$, $\Gamma_c/2\pi = 0{\cdot}048$, $\Gamma/2\pi = 1{\cdot}6$; 1, 2, 3 refer to the three equilibria of Curves 1, 2, 3, respectively (see Figure. 6). (a) Trajectory of vortices obtained by perturbing the equilibria with *symmetric* perturbations. In this (symmetric) subspace, Equilibria 1 and 3 are centers while Equilibrium 2 is a saddle point. One can clearly observe the presence of a homoclinic orbit connecting the saddle to itself. (b) Details of the trajectories of (a). (c-e) Trajectory of vortices obtained by perturbing Equilibrium 1 (c), Equilibrium 2 (d) and Equilibrium 3 (e) with *asymmetric* perturbations showing the instability of Equilibria 1, 2 and the neutral stability of Equilibrium 3 outside the symmetric subspace.

from the various individual equilibria are displayed in Figure 7(c,d,e). While it is clear that the asymmetric perturbations are amplified immediately for Equilibria 1 and 2 [Figure 7(c,d)], the trajectories of Equilibrium 3 remains in a bounded area as shown in Figure 7(e). In the latter case, detailed observation of the latter trajectories shows the asymmetry of the vortices at all times.

The numerical integration of the control model thus confirms the results of our linear stability analysis. One of the most interesting features of the control model is that it generates new equilibrium points, one of which is neutrally stable. Whether a pair of small control vortices can indeed suppress the instability and make a new symmetric bubble stable in the numerically simulated flow is the subject of the next section.

5. NUMERICAL SIMULATIONS OF CONTROLLED FLOWS

The stability analysis of the control vortex model reported in the last section suggests that we may be able to control the wake instability in the real flow by inserting a pair of small symmetric vortices in the flow. In order to pursue this approach, we now carry out two-dimensional numerical simulations of wake flows in the presence of control vortices which play the role of a forcing in the Navier–Stokes equations.

5.1. Control of the Onset of Vortex Shedding at Re = 100

We first investigate whether it is possible to prevent vortex shedding from occurring in the transient flow. For this, we run our code at Re = 100. The transient flow consists of a growing symmetric recirculating bubble of counter-rotating vortices. Under natural conditions, this bubble undergoes a symmetry-breaking instability and evolves toward a Karman vortex street. During the instability events, both the drag and the lift start oscillating, and the drag jumps abruptly to a higher value. In the present computation, the flow is still a recirculating bubble at time $t = 350$. Shortly after this (at time $t = 350{\cdot}01$), we introduce two control vortices $\omega_c = \pm 0{\cdot}2$ at locations $x_c = 4{\cdot}294, y_c = \pm 2{\cdot}031$. Figure 8 displays both the natural evolution of the flow to vortex shedding (left column) and the evolution of the recirculating bubble to another bubble flow under the effect of the control vortices (right column). One clearly observes that the region of strong vorticity in the original bubble is concentrated near the body, while it is more elongated in the controlled flow (right column, compare $t = 350.02$ with $t = 500$).

Figure 9 displays the drag and lift coefficients of the flow in both the uncontrolled case and in the controlled situation. In the uncontrolled flow, Figure 9(a), the drag and the lift start oscillating as the recirculating bubble undergoes the instability, and the drag jumps to a higher value. Here, Algorithm 1 [equation (2)] and Algorithm 2 [equation (3)] of Section 3.1 lead to the same results. In the case of the control, we can compute two types of forces: the forces acting on the body itself via Algorithm 1, and the forces acting on the full system including both the body and the control vortices via Algorithm 2. The selection of a specific control volume does not affect our drag and lift results provided that *cv* is located in a well-resolved area of our computational domain. The forces acting on the body are displayed in Figure 9(b). The first remark is that the force no longer oscillates under the effect of the control. Instead, both the lift and the drag reach constant values after a short transient owing to the steadiness of the asymptotic controlled flow. While the lift remains zero throughout the computation (due to the fact that the flow never loses its reflection symmetry through the mid-plane), the drag increases to a constant value slightly higher than the mean drag value of the vortex shedding. Figure 9(c) presents the body force acting on the system. As in Figure 9(b), the lift remains zero at all times. The drag, however,

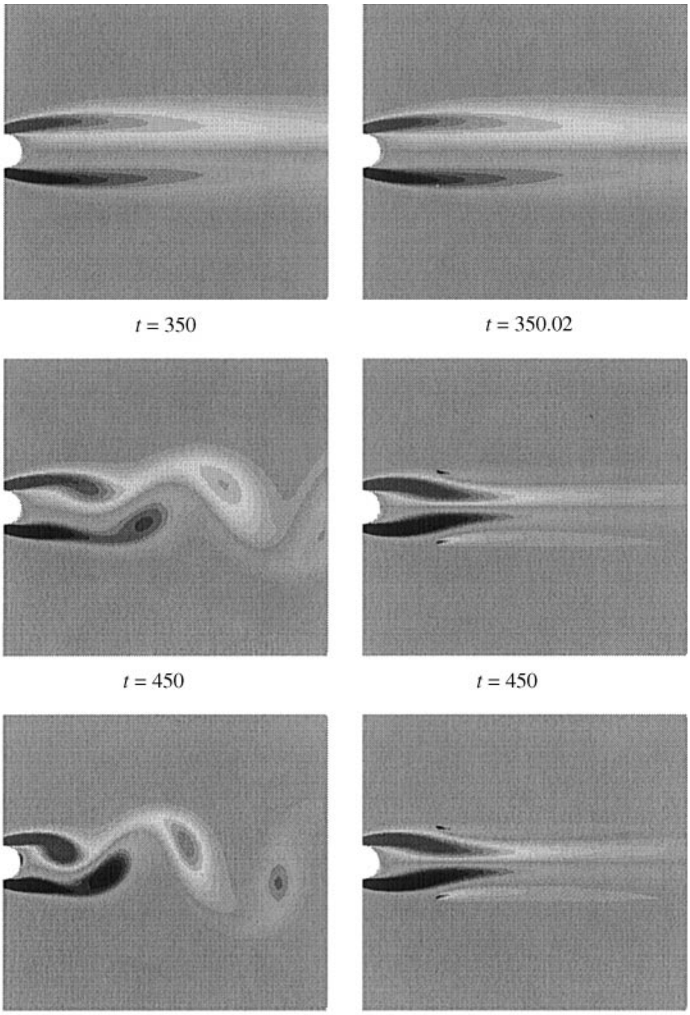

$t = 350$ $t = 350.02$

$t = 450$ $t = 450$

(a) $t = 500$ (b) $t = 500$

Figure 8. Control of the onset of vortex shedding by insertion of two small control vortices ($\omega_c = 0{\cdot}2$) at the location $x_c = 4{\cdot}294$, $y_c = \pm 2{\cdot}031$ at Re = 100, at time $t = 350{\cdot}01$. (a) The flow is visualized by means of vorticity contours. (a) Flow without control, showing the instability of the recirculating bubble; (b) flow with control, showing that the asymptotic state is a symmetric bubble different from the natural bubble (such as that displayed at $t = 350$ in the uncontrolled case).

undergoes a dramatic drop due to the insertion of the control vortices in the flow. After the drop, the drag increases to reach its asymptotic, slightly negative value, showing that the full system experiences weak propulsion. The decrease of the drag acting on the full system can be understood from the relation between the body force and the vorticity distribution in the whole domain:

$$\mathbf{F}_b = -\frac{\mathrm{d}}{\mathrm{d}t}\iint_{\text{fluid}} \mathbf{u}\,\mathrm{d}x\,\mathrm{d}y$$

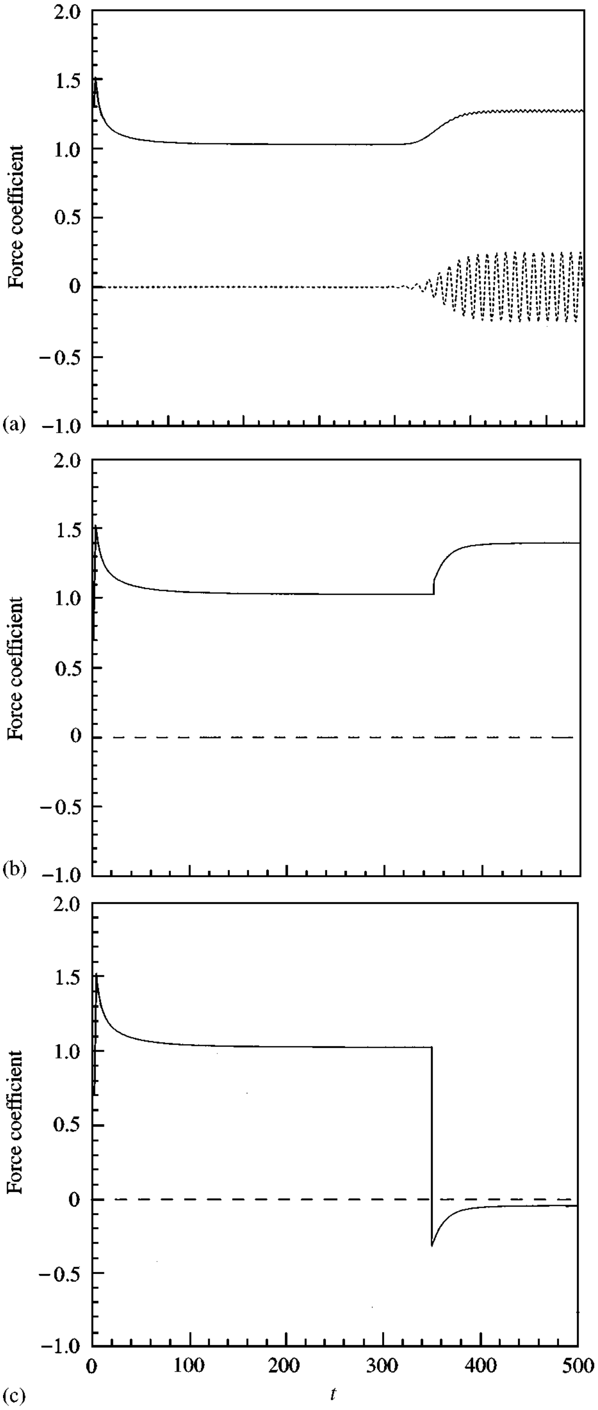

Figure 9. Time history of the force coefficients of the uncontrolled and controlled flows of Figure 8: drag coefficient (solid line), lift coefficient (dashed line). (a) Force coefficients on the body in the uncontrolled flow, (b) force coefficients on the body in the controlled flow, (c) force coefficients on the full system (containing both the cylinder and the control vortices) in the controlled flow.

$$= \frac{\mathrm{d}}{\mathrm{d}t}\iint_{\mathrm{fluid}} \boldsymbol{\omega} \times \mathbf{x}\, \mathrm{d}x\, \mathrm{d}y$$

$$= \frac{\mathrm{d}}{\mathrm{d}t}\iint_{\mathrm{fluid}} (-\omega y \mathbf{i} + \omega x \mathbf{j})\, \mathrm{d}x\, \mathrm{d}y. \tag{30}$$

Here, **i** denotes the direction of the oncoming flow. It is clear from equation (30) that the drag depends only on the time derivative of the integral of $-\omega y$ over the whole flow field. The introduction of new positive (or negative) vorticity at a positive (or negative) y-location decreases the drag. The insertion of the control vortices has no contribution to the lift due to the fact that the effects of the control vortices (of vorticity ω and $-\omega$) cancel each other since they are introduced at the same x-location. The insertion of new vorticity in the flow can thus play a major role in drag-reduction strategies.

5.2. CONTROL OF VORTEX SHEDDING AT Re = 100

We now investigate whether the control technique can destabilize vortex shedding itself after the latter has settled. The flow is the same as that previously described but now we insert the previous control vortices at a much later time ($t = 550{\cdot}01$), more precisely after the Karman vortex street has settled. Figure 10 shows that our control strategy has a significant effect on the flow which is now attracted to an asymptotic stable state consisting of a symmetric bubble. The latter is very similar to that previously obtained by controlling the *onset* of vortex shedding.

Figure 11 displays the corresponding force coefficients. The lift on both the body and the system decays to zero in the presence of the control. The drag on the body slightly increases, while the drag on the system undergoes a significant decrease. As before, the drag value of the asymptotic solution is slightly negative. It is interesting to note that the drag coefficient (on the body) of the asymptotic bubble is $C_d^2 = 1{\cdot}402$ while that obtained by controlling the *onset* of vortex shedding is $C_d^1 = 1{\cdot}401$. The very small relative error between these two values ($\sim 10^{-3}$) confirms the fact that the two asymptotic solutions of Figure 8 (right column) and Figure 10 are the same. This solution constitutes an attractor for the controlled flow whether the initial condition is the recirculating bubble or the Karman vortex street.

5.3. CONTROL OF VORTEX SHEDDING AT Re = 1000

We now investigate whether our control strategy still works at higher Reynolds numbers. For this, we consider Re = 1000. Figure 12 shows the natural vortex shedding, and the evolution of the flow after insertion of the control [$\omega_c = \pm 0{\cdot}8$, at the location $(x_c, y_c) = (2{\cdot}908, \pm 1{\cdot}375)$]. It is interesting to note that soon after the control is turned on, the vortex generated near the body in the upper mid-plane stretches downward as it interacts with the upper control vortex. This stretching process ends by a shedding of this vortex in the lower mid-plane. Likewise, the vortex generated near the body in the lower mid-plane stretches upward before being shed in the upper mid-plane. This dynamics results in a reversed Karman vortex street. The asymmetric bubble consisting of a small vortex and a large one gradually deforms into a symmetric bubble of two counter-rotating vortices of the same size. In the mean time, the intensity of the far wake dynamics decays. It is interesting to concentrate on the final evolution of the asymptotic bubble [see Figure 12(b)]. While large values of vorticity are concentrated in the inner part of the bubble at time

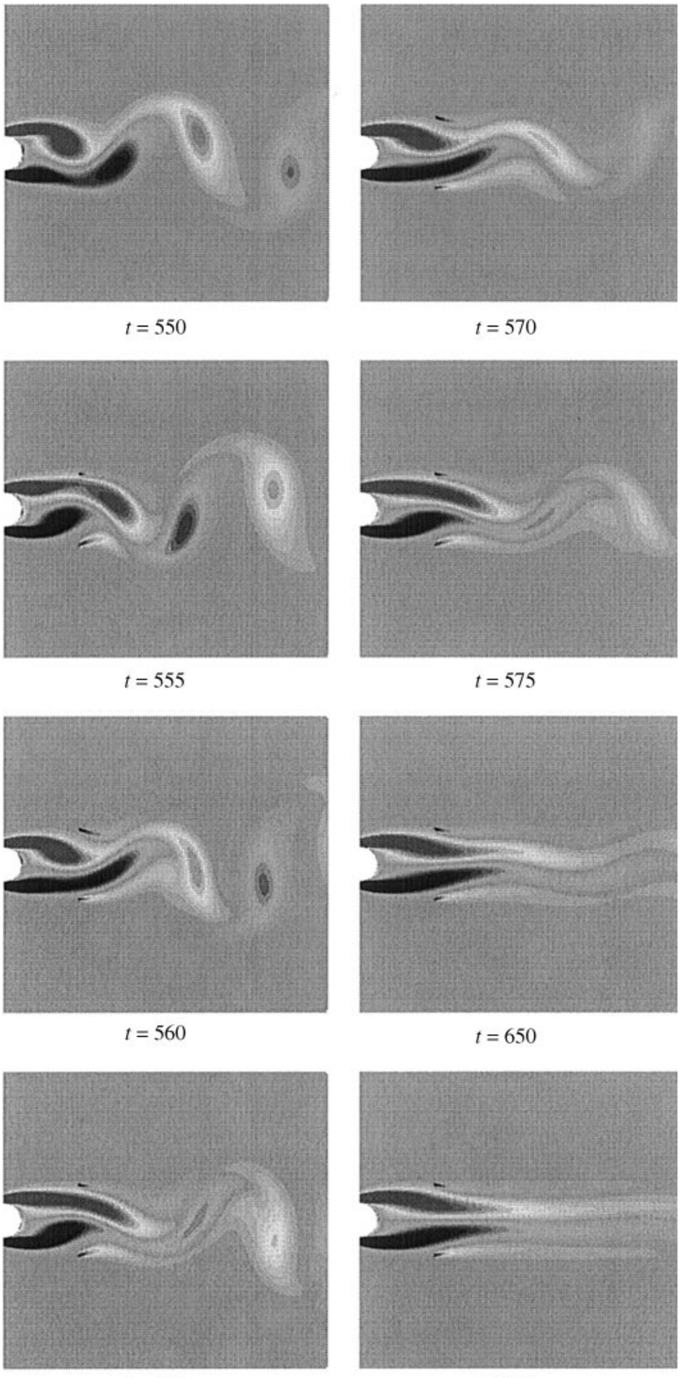

$t = 550$ $t = 570$

$t = 555$ $t = 575$

$t = 560$ $t = 650$

$t = 565$ $t = 750$

Figure 10. Suppression of vortex shedding by insertion of the same small control vortices as in Figure 8. At time $t = 550$, the flow is in its natural vortex shedding state. The control vortices are inserted in the flow at time $t = 550{\cdot}01$. The flow is visualized by means of vorticity contours at various times. The stable asymptotic bubble is very similar to that obtained in Figure 8.

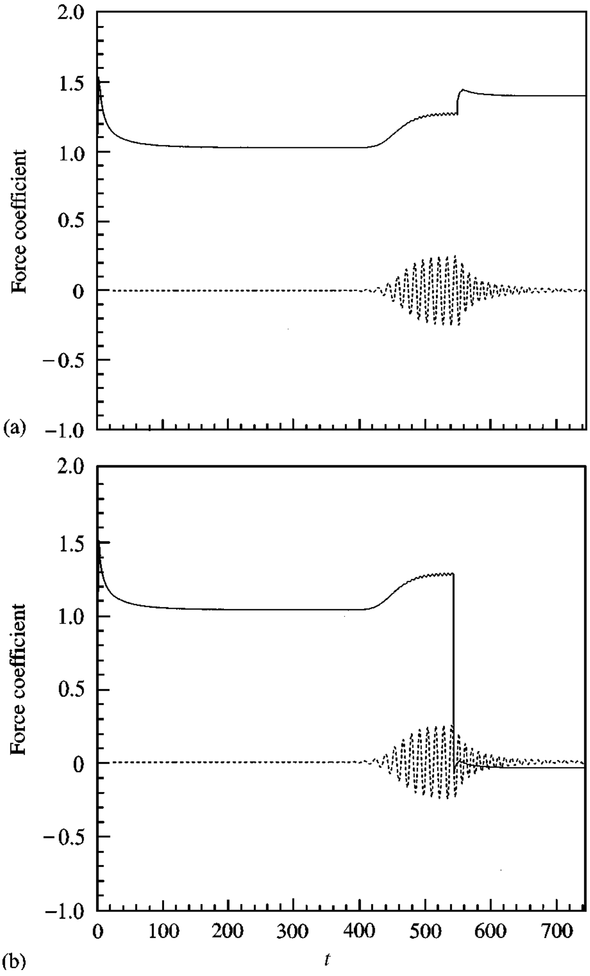

Figure 11. Time history of the force coefficients (a) on the body, (b) on the full system: ——, drag coefficient; – – –, lift coefficient.

$t = 265$, this vorticity decays at later times. At time $t = 360$, high concentrations of vorticity can be found in the shear layers only.

The time history of the force coefficients can be observed in Figure 13. Under the influence of the control, the lift and drag first oscillate during the transient flow, particularly the reversed Karman vortex street. The frequency characteristic of the reversed Karman vortex street is similar to the frequency of the natural vortex shedding. This is consistent with the fact that the reversal of the street originates in the interaction between the shed vortices and the control vortices, and not in the manner the vortices are shed from the body. The lift then decays to zero, while the drag on the body tends to a constant value smaller than the average drag value of the natural vortex shedding. As before, the drag on the system containing both the body and the control vortices decays significantly. The asymptotic negative value is an indicator that propulsion on the full system takes place.

Although the effect of the control persists as the strength and location of the perturbation varies, it is clear that it becomes weaker as the strength of the control vortices decreases. We

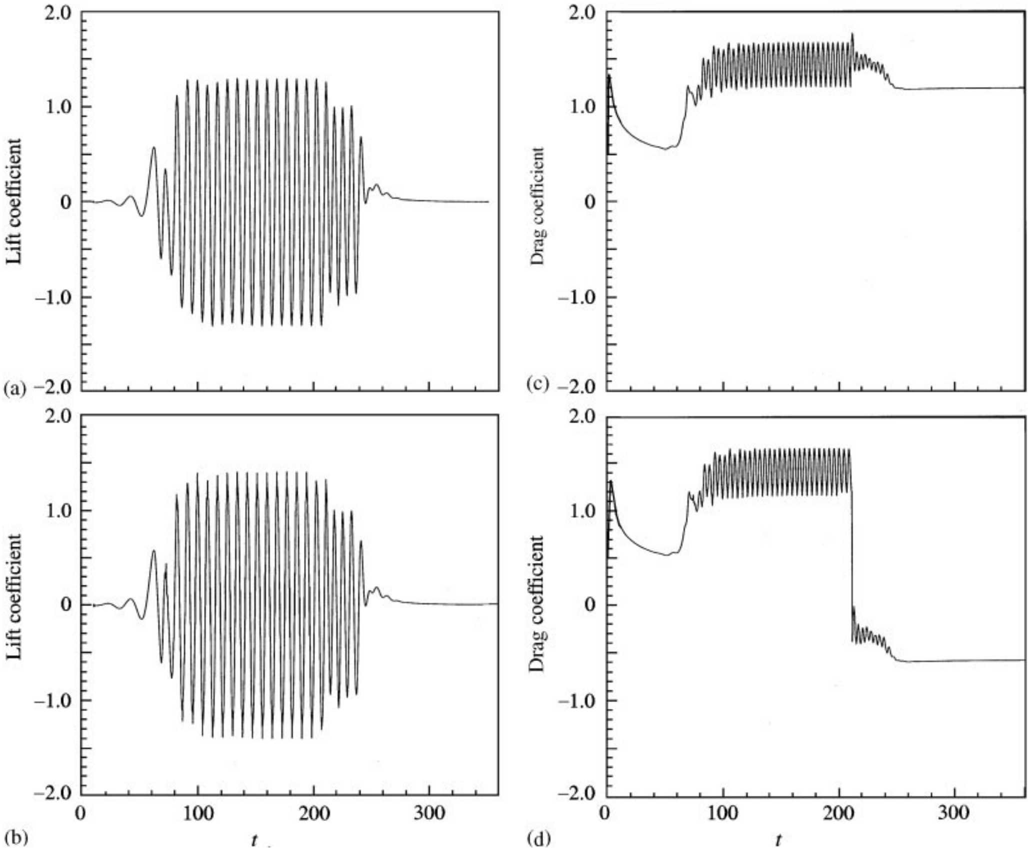

Figure 13. Time history of the force coefficients for the flow visualized in Figure 12: (a) lift coefficient on the body; (b) lift coefficient on the full system; (c) drag coefficient on the body; (d) drag coefficient on the full system.

now introduce the same vorticity in the flow at the same location as before, but with a half vorticity value, that is $\omega_c = 0{\cdot}4$. In this case, the natural Karman vortex street gets deformed into a reversed Karman vortex street through the same physical phenomena as those previously observed in Figure 12. The flow, however, is not attracted to a stable steady state. Fig. 14 visualizes the transient flow at various times and Figure 15 displays the corresponding force coefficients. After insertion of the control vortices, the force still oscillates at the same frequency as before the introduction of the control but the amplitude of the oscillations is smaller.

The introduction of the control vortices ($\omega_c = \pm 0{\cdot}8$) further downstream (at the location ($x_c = 3{\cdot}912, y_c = \pm 1{\cdot}346$)) than in the original experiment has also a weaker effect on the flow as expected. The results are gathered in Figures 16 and 17. In this case, as in the previous one, a reversed Karman vortex street, responsible for asymptotic oscillations of the force coefficients, is obtained. The width of the wake, together with the amplitude of the oscillations, seem to be larger than that observed in Figures 15 and 16.

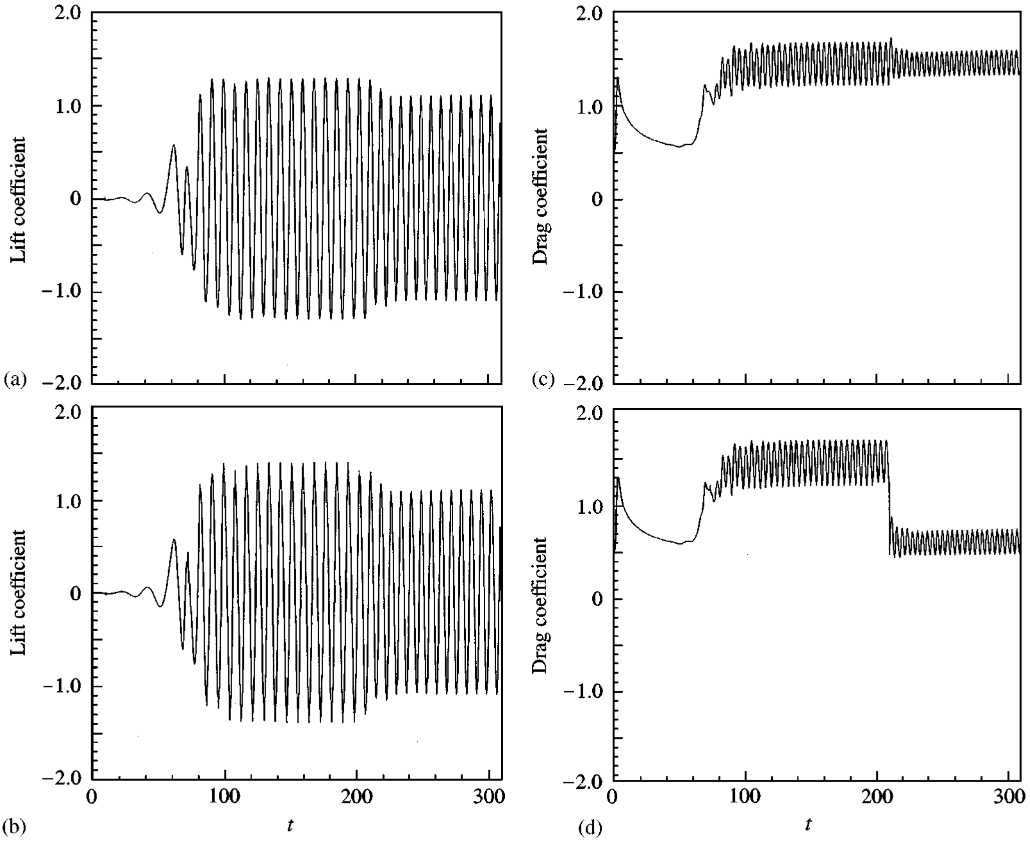

Figure 15. Time history of the force coefficients for the flow visualized in Figure 14: (a) lift coefficient on the body; (b) lift coefficient on the full system; (c) drag coefficient on the body; (d) drag coefficient on the full system.

6. CONCLUSIONS

In this paper, we have developed a flow control approach for the manipulation of the wake flow past a circular cylinder above the critical Reynolds number. Our control strategy was inspired by the stability analysis of the low-dimensional point vortex model originally derived by Föppl. In the model, the instability of the twin vortices was controlled by introducing an additional pair of point vortices, referred to as *control vortices*, for which the circulation is kept small compared with the circulation of the twin vortices. The insertion of extra point vortices generates additional steady (symmetric) *bubble* solutions, one of which being neutrally stable (rather than unstable). The insertion of additional sources of vorticity was also found to be efficient in controlling the viscous flow. In the latter case, the vortex-shedding regime never develops if additional (control) vorticity is inserted in the flow before symmetry breaking occurs. We have also shown that our control strategy destabilizes the Karman vortex street, making the flow converge toward a steady, stable bubble solution. In two dimensions, this technique was found to work at small Reynolds number (Re = 100) and at relatively high Reynolds number (Re = 1000). In the case of a weaker control (the vorticity of the control vortices is smaller or the control vortices are located farther downstream), the Karman vortex street is reversed.

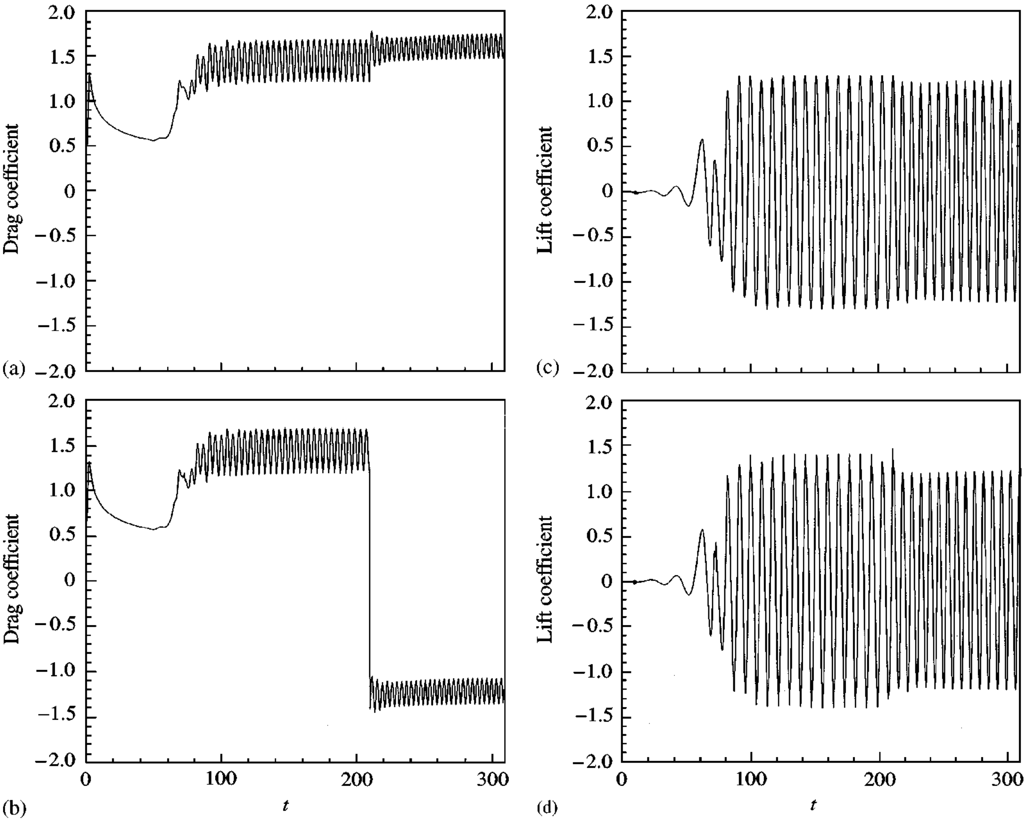

Figure 17. Time history of the force coefficients on the cylinder: (a) lift coefficient on the body; (b) drag coefficient on the system; (c) drag coefficient on the body; (d) drag coefficient on the system.

One may wonder how small the strength of the control vortices in the viscous flow is, compared to that of the twin vortices. In order to address this issue, we consider the asymptotic controlled bubble flow. Since this state is symmetric by reflection through the centerline, our estimate is restricted to the upper half-plane only. We first determine the point located on the surface of the body such that the vorticity is zero (separation point). This point defines a *separation angle* with the centerline. We then consider the portion P of the wake located within the separation angle. In this part of the domain, we associate all *negative* vorticity with the twin vortex, and all *positive* vorticity with the control vortex. In each vortex, we then determine the maximal vorticity value (in absolute value) which we denote $|\omega^t_{\max}|$ for the twin vortex, and $|\omega^c_{\max}|$ for the control vortex. We then compute the circulation corresponding to all *negative* vorticity such that $|\omega| > 0{\cdot}1|\omega^t_{\max}|$ for all points in P. This gives us an estimate of the circulation characteristic of the upper twin vortex, Γ_t. In order to estimate the circulation associated with the control vortex, Γ_c, we proceed in the same manner and compute the circulation corresponding to all *positive* vorticity such that $|\omega| > 0{\cdot}1|\omega^c_{\max}|$. For the controlled bubble obtained at Re = 100, we find that $\Gamma_t = 8.79$ and $\Gamma_c = 0{\cdot}25$, thus leading to a ratio $\Gamma_c/\Gamma_t = 0{\cdot}028$. For the controlled bubble obtained at Re = 1000, we obtain $\Gamma_t = 10{\cdot}75$ and $\Gamma_c = 1{\cdot}11$, thus leading to a ratio $\Gamma_c/\Gamma_t = 0{\cdot}10$. It is clear that we have not optimized our control technique. Particularly at Re = 1000, it should be possible to decrease the ratio Γ_c/Γ_t below 10%.

Despite the similarity between the stability characteristic of the potential model and that of the viscous flow, we refrain ourselves from extending our comparison between the model and the numerically simulated flow further. In particular, it is well-known that the vortices present in the viscous flow are very different from point vortices. It is, however, somewhat intriguing that the neutrally stable equilibrium of the controlled model is located farther downstream than the unstable equilibria. This qualitative feature persists in the viscous flow in the sense that the asymptotic controlled bubble flow has most of its vorticity concentrated in the shear layers. This high concentration of vorticity thus extends farther downstream than in the uncontrolled bubble. This discrepancy between the naturally growing bubble and the asymptotic controlled bubble can be clearly observed in Figure 18 which shows the asymptotic flow of Figure 13 in a slightly different manner.

Obviously, there is a need for investigating whether the efficiency of the control technique developed in this paper will persist in three-dimensional simulations, as well as in experiments, particularly at high Reynolds numbers ($\mathrm{Re} > 180$ or so) at which the flow is known to be three-dimensional. This question will be addressed in future work. In practice, the vortex generator could be a small airfoil or a small rotating cylinder. In any case, the efficiency of the presence of small vortices in controlling the flow has shown how a small *local* change can have major *global* consequences on wake flows.

REFERENCES

AUBRY, N., HOLMES, P., LUMLEY, J. L. & STONE, E. 1988 The dynamics of coherent structures in the wall region of a turbulent boundary layer. *Journal of Fluid Mechanics* **192,** 115–172.

AUBRY, N. & LIMA, R. 1995 Spatio-temporal and statistical symmetries. *Journal of Statistical Physics* **81,** 793–828.

AUBRY, N., LIMA, R. & GUYONNET, R. 1992 Spatio-temporal symmetries and bifurcations via biorthogonal decompositions. *Journal of Nonlinear Science* **2,** 183–215.

BAR-LEV, M. & YANG, H. T. 1975 Initial flow field overt an impulsively started circular cylinder. *Journal of Fluid Mechanics* **72,** 625–647.

BEARMAN, P. W. 1967 The effect of base bleed on the flow behind a two-dimensional model with a blunt trailing edge. *Aeronautical Quaterly* **18,** 207–224.

BERGER, E. 1967 Suppression of vortex shedding and turbulence behind oscillating cylinders. *Physics of Fluids Supplement* **10,** 191–193.

COLLER, B. D., HOLMES, P. & LUMLEY, J. L. 1994 Control of bursting in boundary layer models. *Applied Mechanics Reviews* **47,** part 2, S139–143.

COLLINS, W. M. & DENNIS, S. C. R. 1973 The initial flow past an impulsively started circular cylinder. *Quarterly Journal of Mechanics and Applied Mathematics* **26,** 53–75.

CORTELEZZI, L. 1996 Nonlinear feedback control of the wake past a plate with a suction point on the downstream wall. *Journal of Fluid Mechanics* **327,** 303–324.

CORTELEZZI, L., LEONARD, A. & DOYLE, J. C. 1994 An example of active circulation control of the unsteady separated flow past a semi-infinite plate. *Journal of Fluid Mechanics* **260,** 127–154.

FFOWCS WILLIAMS, J. E. & ZHAO, B. C. 1989 The active control of vortex shedding. *Journal of Fluids and Structures* **3,** 115–122.

FÖPPL, L. 1913 Wirbelbewegung hinter einem Kreiszylinder. *Sitzungsberichte der Bäyerischen Academie der Wissenschaften*, 1–17.

FRANKE, R., RODI, W. & SCHONUNG, B. 1990 Numerical calculation of laminar vortex shedding flow past cylinders. *Journal of Wind Engineering and Industrial Aerodynamics* **35,** 237–257.

GAD-EL-HAK, M. 1999 *Flow Control: Passive, Active and Reactive Flow Management*. Cambridge: Cambridge University Press, to be published.

GOPALKRISHNAN, R., TRIANTAFYLLOU, M. S., TRIANTAFYLLOU, G. S. & BARRETT, D. 1994 Active vorticity control in a shear flow using a flapping foil. *Journal of Fluid Mechanics* **274,** 1–21.

GROVE, A. S., SHAIR, F. H., PETERSEN, E. E. & ACRIVOS, A. 1964 An experimental investigation of the steady separated flow past a circular cylinder. *Journal of Fluid Mechanics* **19,** 60–80.

HENDERSON, R. D. 1994 Unstructured spectral element methods: parallel algorithms and simulations. Ph.D. thesis, Princeton University.

Mori, Y., Hijikata, K. & Nobuhara, T. 1986 A fundamental study of symmetrical vortex generation behind a cylinder by wake heating or by splitter plate or mesh. *International Journal of Heat and Mass Transfer* **29,** 1193–1201.

Noto, K., Ishida, H. & Matsumoto, R. 1985 A breakdown of the Karman vortex street due to the natural convection. In *Flow Visualization III* (ed. W. J. Yang), pp. 348–352. Washington, DC:Hemisphere.

Roshko, A. 1955 On the wake and drag of bluff bodies. *Journal of Aeronautical Science* **22,** 124–132.

Roussopoulos, K. 1993 Feedback control of vortex shedding at low Reynolds numbers. *Journal of Fluid Mechanics* **248,** 267–296.

Sanghi, S. & Aubry, N. 1993 Interaction mode models of near wall turbulence. *Journal of Fluid Mechanics* **247,** 455–488.

Schumm, M. S., Berger, E. & Monkewitz, P. A. 1994 Self-excited oscillations in the wake of two-dimensional bluff bodies and their control. *Journal of Fluid Mechanics* **271,** 17–53.

Strykowski, P. J. & Sreenivasan, K. R. 1990 On the formation and suppression of vortex 'shedding' at low Reynolds numbers. *Journal of Fluid Mechanics* **218,** 71–107.

Strykowski, P. J. & Hannemann, K. 1991 Temporal simulation of the wake behind a circular cylinder in the neighborhod of the critical Reynolds number. *Acta Mechanica* **90,** 1–20.

Tang, S. & Aubry, N. 1997 On the symmetry breaking instability leading to vortex shedding. *Physics of Fluids* **9,** 2550–2561.

Tokumaru, P. T. & Dimotakis, P. E. 1991 Rotary oscillation control of a cylinder wake. *Journal of Fluid Mechanics* **224,** 77–90.

Tritton, D. J. 1959 Experiments on the flow past a circular cylinder at low Reynolds numbers. *Journal of Fluid Mechanics* **6,** 547–567.

Wehrmann, O. H. 1965 Reduction of velocity fluctuations in a Karman vortex street by a vibrating cylinder. *Physics of Fluids* **8,** 760–761.

Williamson, C. H. K. 1995 Vortex dynamics in the wake of a cylinder. In *Fluid Vortices* (ed. S. I. Green), Dordrecht: Kluwer Academic Publishers.

Wood, C. J. 1967 Visualization of an incompressible wake with base bleed. *Journal of Fluid Mechanics* **29,** 259–272.

Zdravkovich, M. M. 1981 Review and classification of various aerodynamic and hydrodynamic means for suppressing vortex shedding. *Journal of Wind Engineering and Industrial Aerodynamics* **7,** 145–189.

Zhang, H. Q., Fey, U. & Noack, B. R. 1995 On the transition of the cylinder wake. *Physics of Fluids* **7,** 779–794.

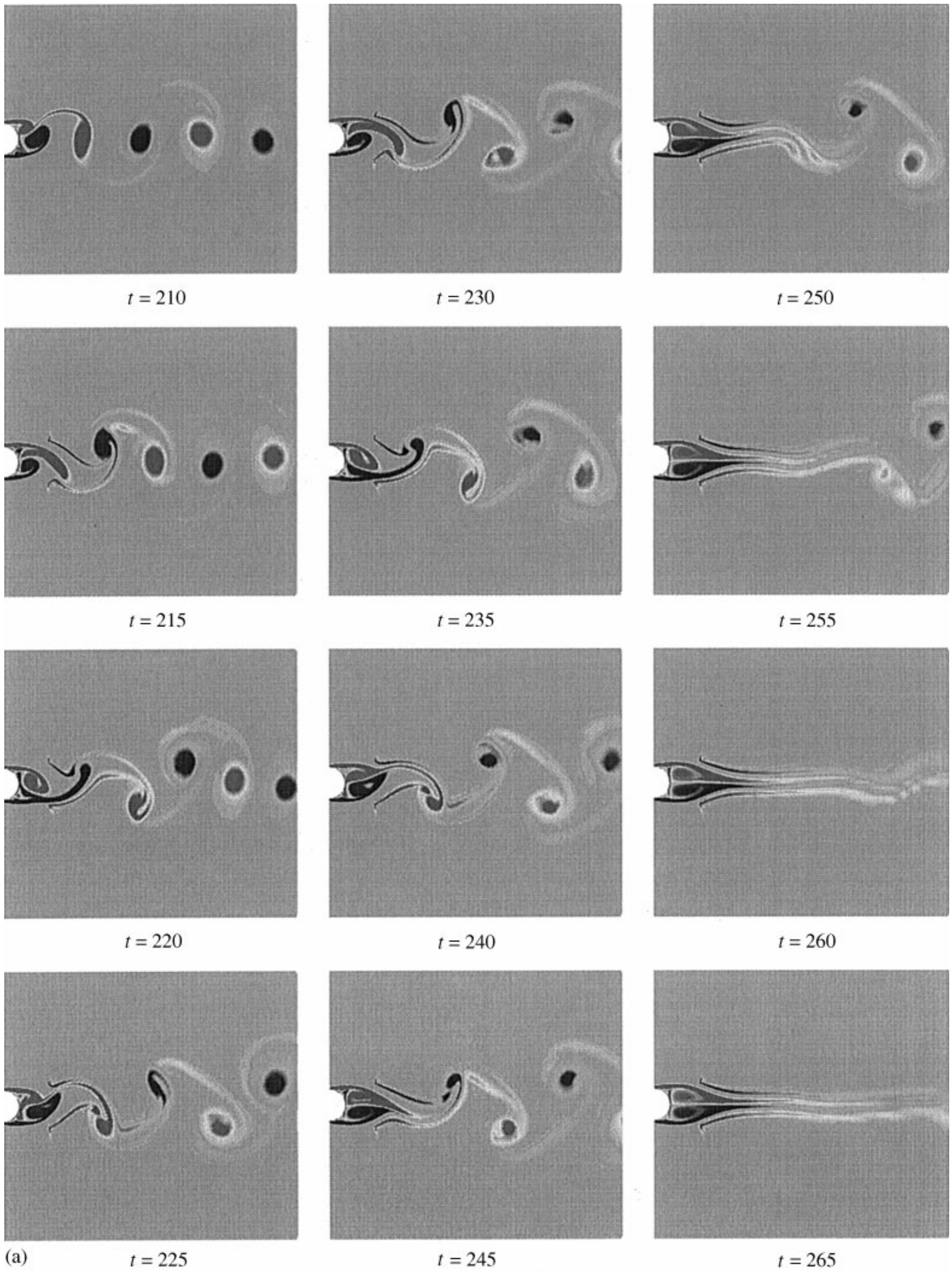
$t = 210$ $t = 230$ $t = 250$

$t = 215$ $t = 235$ $t = 255$

$t = 220$ $t = 240$ $t = 260$

(a) $t = 225$ $t = 245$ $t = 265$

Figure 12. Suppression of vortex shedding by insertion of two small control vortices ($\omega_c = 0{\cdot}8$) at the location $x_c = 2{\cdot}908$, $y_c = \pm 1{\cdot}375$ at $\mathrm{Re} = 1000$. At time $t = 210$, the flow is in its natural vortex-shedding state. The control vortices are inserted in the flow at time $t = 210{\cdot}01$. The flow is visualized by means of vorticity contours at various times: (a) visualizations of the flow showing the evolution of the Karman vortex street; (b) visualizations of the flow showing the late evolution of the bubble toward its asymptotic state.

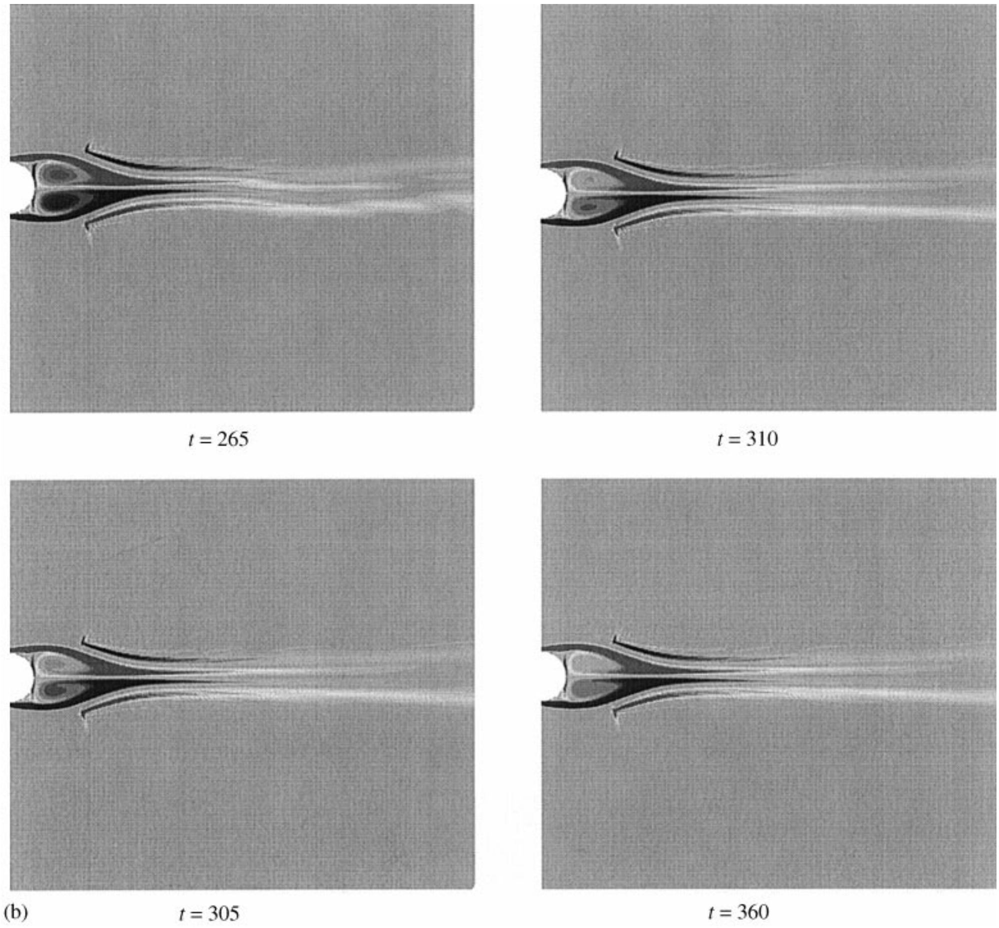

Figure 12 (*Continued*).

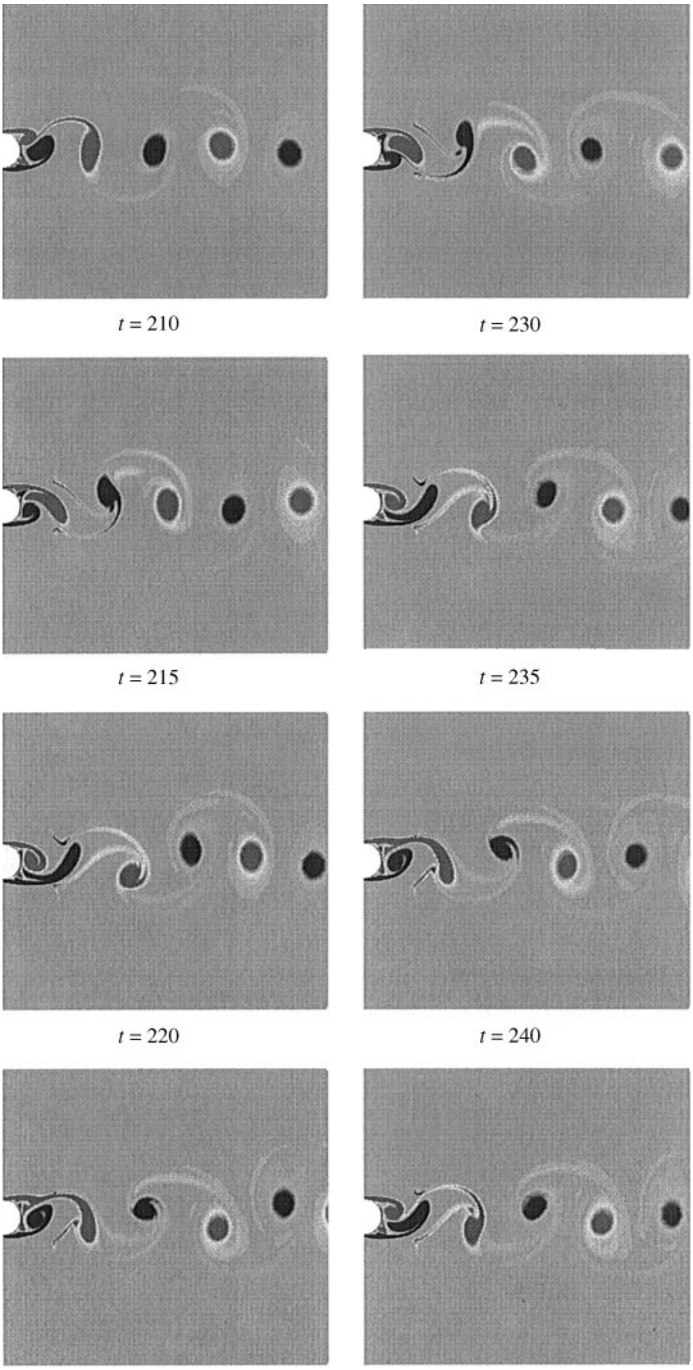

$t = 210$

$t = 215$

$t = 220$

$t = 225$

$t = 230$

$t = 235$

$t = 240$

$t = 310$

Figure 14. Alteration of vortex shedding by insertion of two small control vortices ($\omega_c = 0{\cdot}4$) at the location $x_c = 2{\cdot}908$, $y_c = \pm 1{\cdot}375$ at $\mathrm{Re} = 1000$. The control vortices are inserted in the flow at the same time as in Figure 12. The flow is visualized by means of vorticity contours at various times. The asymptotic state of the flow is a reversed Karman vortex street.

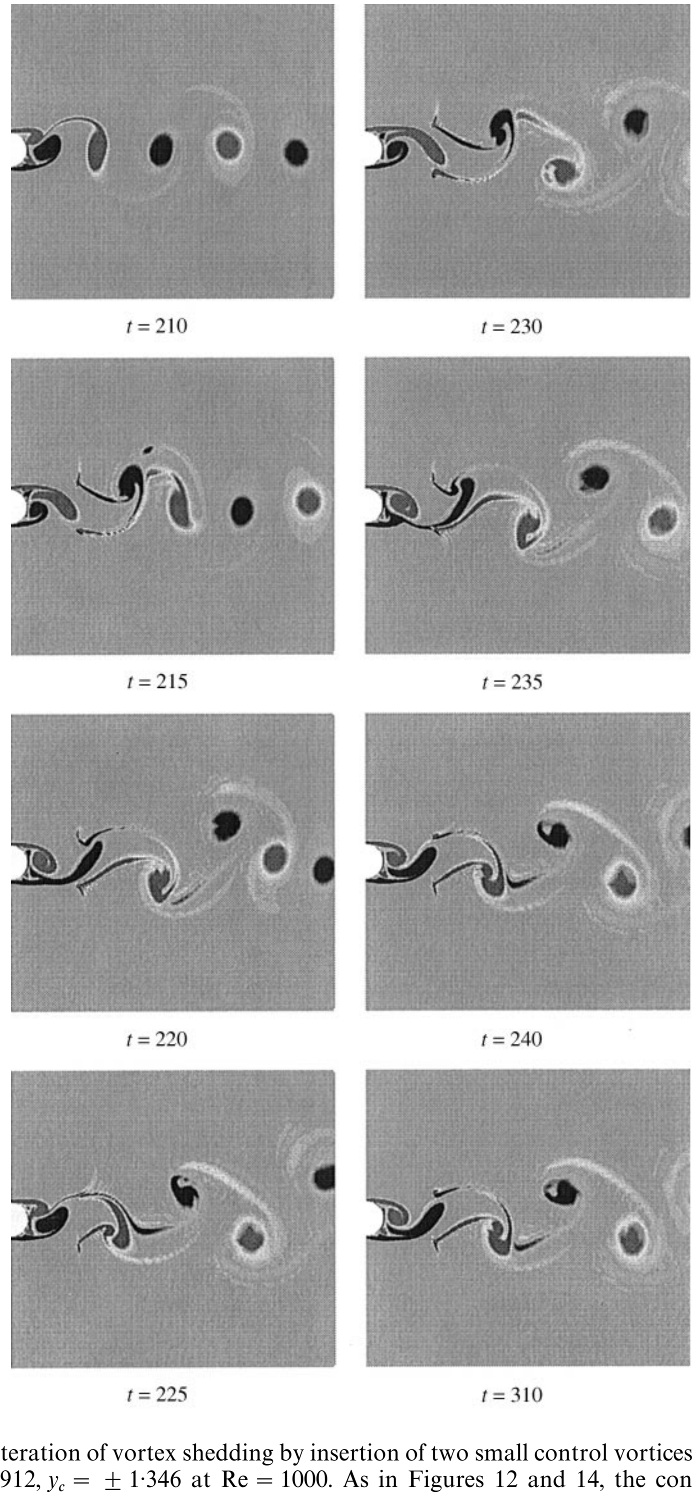

$t = 210$ $t = 230$

$t = 215$ $t = 235$

$t = 220$ $t = 240$

$t = 225$ $t = 310$

Figure 16. Alteration of vortex shedding by insertion of two small control vortices ($\omega_c = 0{\cdot}8$) at the location $x_c = 3{\cdot}912$, $y_c = \pm 1{\cdot}346$ at Re = 1000. As in Figures 12 and 14, the control vortices are inserted in the flow at time $t = 210{\cdot}01$. The flow is visualized by means of vorticity contours at various times. As in Figure 14, the asymptotic state is a reversed Karman vortex street.

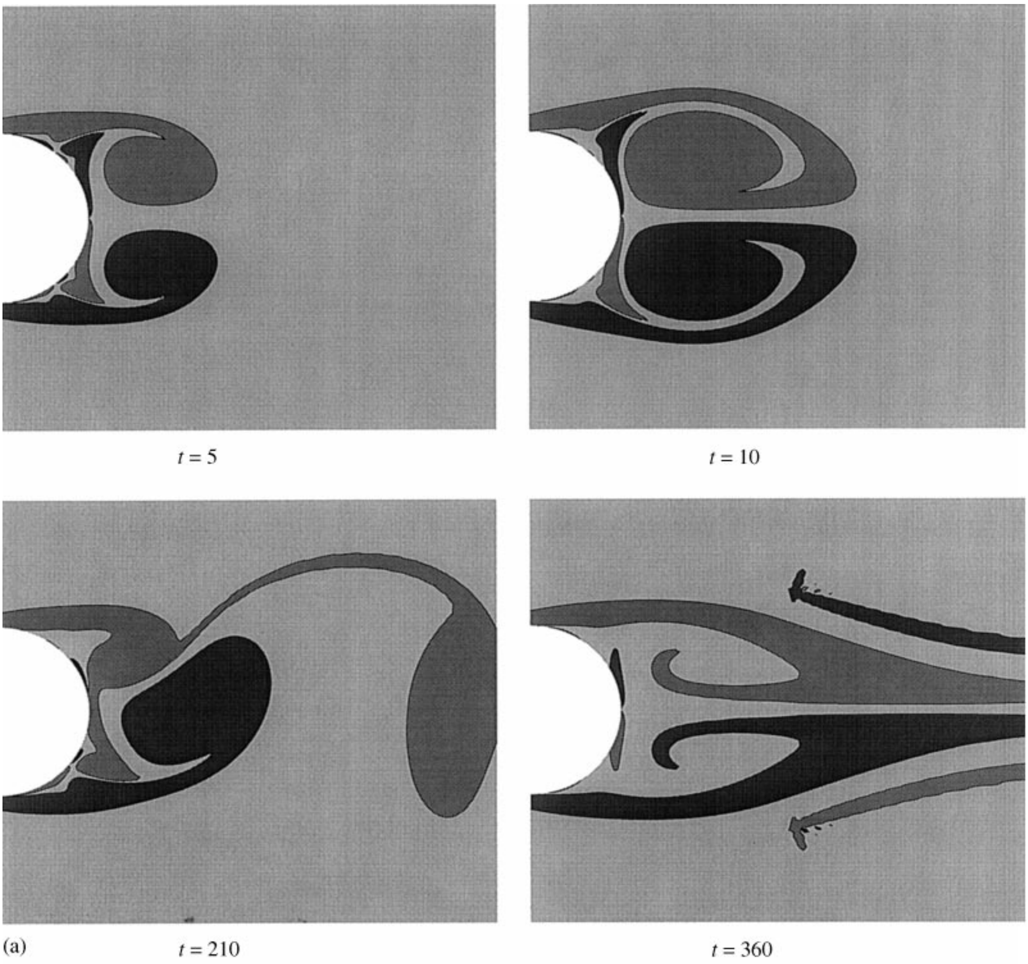

(a) $t = 5$ $t = 10$ $t = 210$ $t = 360$

Figure 18. Regions of positive and negative vorticity for the flow displayed in Figure 12(b) at time $t = 360$: (a)$|\omega| \geq 1{\cdot}5$; (b) $|\omega| \geq 2{\cdot}0$.

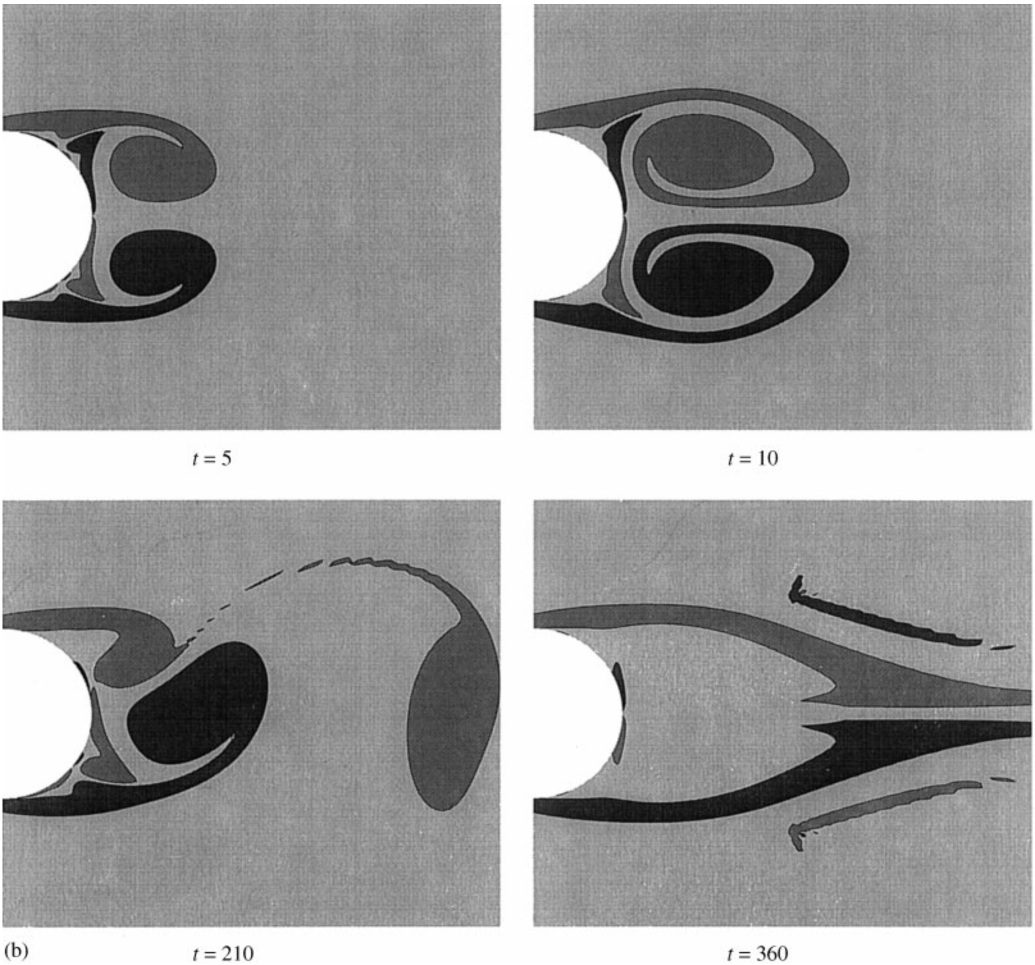

Figure 18 (*Continued*).